

The Correlation Between Tropical Convection and Upper Tropospheric Momentum Flux Convergence

Matthew T. Boehm

National Research Council
Washington, DC 20418

David O'C. Starr

NASA Goddard Space Flight Center
Greenbelt, MD 20771

July 31, 2003

The Correlation Between Tropical Convection and Tropical Upper Tropospheric Momentum Flux Convergence

Matthew T. Boehm and David O'C. Starr

Popular Summary

In the deep Tropics, the air in the upper troposphere and lower stratosphere is slowly rising at a rate of a few tens of meters per day. Although this rising motion plays important roles in the vertical transport of water vapor and other chemicals into the tropical stratosphere, its cause is not completely understood. It is likely that several mechanisms work together to generate the rising motion. A key component of one such mechanism is investigated in this article.

According to the mechanism considered here, large, organized regions of thunderstorms in the Tropics, also known as tropical convection, generate waves in the wind fields of the tropical upper troposphere. These waves transport eastward momentum into the deep Tropics, leading to a convergence of eastward momentum in this region. This convergence, in turn, tends to generate an eastward acceleration of the wind. However, in spite of this acceleration, the winds in the tropical upper troposphere are generally light and steady. Part of the resolution of this apparent discrepancy involves the generation of rising motion in the tropical upper troposphere and lower stratosphere.

In this article, the focus is on the relationship between tropical convection and the convergence of eastward momentum. This relationship is investigated using global data sets related to both tropical convection and momentum convergence. Tropical convection is represented by outgoing longwave radiation (OLR) data from satellites. The amount of radiation emitted by clouds, and therefore measured by the satellite, depends on the temperature near the top of the clouds. Since the clouds associated with tropical convection have high cloud tops with cold temperatures, tropical convection is characterized by low values of OLR. The convergence of eastward momentum is calculated beginning with wind data from a global data set.

The relationship between the OLR and momentum convergence data sets is quantified through the calculation of correlation coefficients between the two quantities on both the yearly and daily time scales. To see how the relationship varies over the course of the year, calculations were carried out for each of the four seasons individually. In general, the results reveal a high degree of correlation over a portion of the deep Tropics during each season, showing that there is indeed a close relationship between organized tropical convection and the convergence of eastward momentum in the tropical upper troposphere. The regions covered by high values of correlation, as well as the peak correlation values calculated for these regions, vary with season. Finally, the correlation patterns obtained suggest that a significant portion of the momentum convergence in the tropical upper troposphere is generated by a specific type of wave known as the mixed Rossby-gravity wave.

Abstract

In this study, the relationship between tropical convection and the meridional convergence of zonal momentum flux in the tropical upper troposphere is investigated using NOAA interpolated outgoing longwave radiation data and NCEP-NCAR reanalysis wind data. In particular, a variety of correlation coefficients are calculated between the two data sets, both of which are filtered to isolate disturbances with frequencies and wavenumbers consistent with the Madden-Julian oscillation. The results show regions of significant correlation during each season, with the magnitude and area covered by significant correlation coefficients varying with season. Furthermore, it is found that the correlation structures look very similar to theoretical calculations of the atmospheric response to a region of tropical heating. This result suggests that tropical waves, in particular mixed Rossby-gravity waves, play an important role in the meridional transport of zonal momentum into the deep tropical upper troposphere. Finally, these findings have implications to the generation of rising motion near the tropical tropopause, which in turn has ramifications for vertical moisture transport and tropopause cirrus formation.

1. Introduction

The meridional convergence of zonal eddy momentum flux, $-\frac{\partial u'v'}{\partial y}$, (momentum flux convergence, hereafter) in the upper troposphere of the deep Tropics (approximately 10°S-10°N) plays a role in the dynamics of the tropical upper troposphere and lower stratosphere. Lee (1999) shows that the net momentum flux convergence is positive in the equatorial upper troposphere, indicating that, in this region, eddy-momentum fluxes of tropical-origin dominate those of midlatitude-origin. Furthermore, it is shown that the spatial and temporal scales of the waves responsible for this momentum flux convergence are consistent with those of the El Niño-Southern Oscillation (ENSO) and the Madden-Julian Oscillation (MJO; Madden and Julian 1971, 1972), suggesting that the momentum flux convergence in the tropical upper troposphere is ultimately driven by tropical convective heating.

Starting with the results of Lee (1999), Boehm and Lee (2003) show that momentum flux convergence in the equatorial upper troposphere may play an important role in producing upwelling in the tropical upper troposphere and lower stratosphere. A limitation of the work of Boehm and Lee (2003) is that they used a zonal-mean dynamics model with momentum flux convergence represented by multi-year monthly mean quantities. Therefore, they could not explore the impact of longitudinal and temporal variability in momentum flux convergence on rising motion.

However, tropical convection clearly exhibits significant longitudinal and temporal variability, so it is expected that the momentum flux convergence generated in response to convection will similarly vary. This variability in momentum flux convergence, in turn, will lead to similar variability in the rising motion generated by the hypothesis presented in Boehm and Lee (2003). Here, we explore the spatial and temporal variability in both outgoing longwave

radiation and momentum flux convergence in detail, with an emphasis on using this variability to look at the connection between momentum flux convergence and tropical convective heating established by Lee (1999).

2. Data

Since the primary purpose of this paper is to study the connection between tropical convection and upper tropospheric momentum flux convergence, data related to both quantities are needed. As has been done in a number of previous studies, outgoing longwave radiation (OLR) is used as a proxy for tropical convection (e.g. Gruber 1974; Hendon and Liebmann 1991; Wheeler and Kiladis 1999; Gu and Zhang 2001). The OLR data set used here is the 2.5° resolution daily interpolated OLR data set produced by the NOAA CIRES Climate Diagnostics Center (Gruber and Krueger 1984; Liebmann and Smith 1996). Momentum flux convergence at 150 mb is calculated from National Centers for Environmental Prediction-National Center for Atmospheric Research (NCEP-NCAR) reanalysis daily zonal and meridional wind data, from which the seasonal cycle has been subtracted. Both the OLR and convergence data sets are filtered to focus on the low zonal wavenumber, low frequency variability associated with the Madden-Julian oscillation (MJO), since it has been shown that momentum flux convergence in the tropical upper troposphere is strongest at MJO wavenumbers and frequencies (Lee 1999). The details of this filtering are given in the next section, along with a description of the method used to calculate momentum flux convergence.

3. Filtering and convergence calculations

Both the OLR and deseasonalized wind data are filtered to isolate variability associated with MJO frequencies and zonal wave numbers. For each latitude and pressure level under consideration, the first step in the filtering process is to produce a 90-day longitude-time cross-section, $X(\lambda, t)$, where λ and t represent longitude and time, respectively. Next, the combined wavelet-fft analysis technique described by Gu and Zhang (2001) is applied to this cross section, yielding the Fourier transform of the wavelet transform of X , denoted $\hat{X}^*(k, \lambda, \omega)$, where the “hat” and asterisk indicate the wavelet and Fourier transforms, respectively, and k and ω represent zonal wavenumber and frequency, respectively. Finally, the MJO-filtered data, X_{MJO} , are produced by performing the inverse wavelet and Fourier transforms over the range of coefficients $k=1-2$ and $\omega=0.011-0.044 \text{ day}^{-1}$, which is representative of the MJO.

Combining the filtered data from a range of latitudes results in daily maps of the MJO-filtered OLR, zonal wind, and meridional wind, denoted by OLR_{MJO} , U_{MJO} , and V_{MJO} , respectively. Example maps of OLR_{MJO} are shown in Fig. 1a-d. These maps, spaced 15 days apart, show a typical MJO event. A region of negative OLR_{MJO} associated with the active phase of the MJO propagates slowly eastward from the Indian Ocean on 30 December 1989 (Fig. 1a), to the eastern Pacific Ocean on 13 February 1990 (Fig. 1d). Figure 1e shows a Hovmuller diagram (longitude-time cross section) at 5°S of OLR_{MJO} for Dec. 1989 through Feb. 1990, the season shown in Figs. 1a-d. This diagram further illustrates the eastward-propagating structures associated with the MJO. Maps similar to Figs. 1a-d were produced for each day of each season over the 20-year period Dec. 1982 through Nov. 2002, and the seasons are designated by DJF (December 1-February 28), MAM (March 1-May 29), JJA (June 1-August 29), and SON (September 1-November 29). The maps presented in Figs. 1a-d closely resemble the OLR

anomaly maps presented by Wang and Rui (1990), in which the data represent variations on temporal scales from 10 to 90 days and zonal wavenumber 1 to 6.

The MJO-filtered meridional convergence of zonal momentum flux, $\frac{-\partial u'v'}{\partial y}_{MJO}$, is calculated in grid-point space from U_{MJO} and V_{MJO} . In this paper, all references to $\frac{-\partial u'v'}{\partial y}_{MJO}$ are at 150 mb, which is near the level of maximum momentum flux convergence in the tropical upper troposphere (see Fig. 3 in Boehm and Lee (2003)). Examples of $\frac{-\partial u'v'}{\partial y}_{MJO}$ are shown in Fig. 2 for the same days and season presented in Fig. 1. Eastward propagating structures in $\frac{-\partial u'v'}{\partial y}_{MJO}$ are not as clearly visible in Figs. 2a-d as they were for OLR_{MJO} in Figs. 1a-d.

However, such structures are very evident in Fig. 2e. Meridional fluxes of zonal momentum in association with the MJO have been described in several previous studies (e.g. Chen 1985; Madden 1986; Madden and Julian 1986). However, we are not aware of any previous gridpoint calculations of MJO-related upper tropospheric zonal momentum flux convergence.

A quick comparison of Figures 1e and 2e suggests that OLR_{MJO} and $\frac{-\partial u'v'}{\partial y}_{MJO}$ are related to each other. This one season of data is not adequate for establishing a correlation between these two variables. The remainder of this article focuses on establishing and quantifying this correlation.

4. Long-term seasonal means

An examination of analyses like Figures 1 and 2 for each season over the 20-year period reveals that the strength and frequency of occurrence of structures in both OLR_{MJO} and

$\frac{-\partial u'v'}{\partial y}_{MJO}$ depend on location, and that the location of the strongest and most frequent structures varies with season. To determine the locations where MJO-related structures are most prevalent, long-term (20-year) means of *unfiltered OLR*, OLR_{MJO}^2 , and $\frac{-\partial u'v'}{\partial y}_{MJO}$ for each season are presented in this section. The long-term means of filtered OLR are calculated based on the MJO-filtered OLR *power*, OLR_{MJO}^2 , since the filtering procedure yields OLR_{MJO} with time means equal to zero.

a. Outgoing longwave radiation

Figure 3 shows the 20-year mean unfiltered OLR for each season. Low values of OLR in the tropics are indicative of extensive high, cold clouds associated with tropical convection. In each season, there are 3 primary regions of low OLR: one over South America, another over Africa, and the third over Micronesia. The latitudes of OLR minima tend to shift north and south with the seasons, following the sun. The OLR minima are generally south of the equator in DJF (Fig. 3a), north of the equator in JJA (Fig. 3c) and relatively near the equator in MAM (Fig. 3b) and SON (Fig. 3d). The intertropical convergence zone (ITCZ) is visible as a band of low OLR extending across the Pacific Ocean just north of the equator. It is most prominent during SON (minimum OLR $< 220 \text{ W m}^{-2}$), slightly weaker during JJA, somewhat weaker still during MAM, and virtually nonexistent during DJF. The South Pacific convergence zone (SPCZ), which extends southeastward from Micronesia into the western South Pacific, shows less seasonal variability in size and strength than the ITCZ. A couple of additional features are relevant to the results to be presented later. The first is the southeast Asian monsoon, which is prominent as a significant reduction in OLR over India and southeast Asia during both JJA and SON. The other

is the region of reduced OLR in extreme northwest South America, extending northwestward along the western coast of Central America; this feature is most prominent in JJA, and is also apparent in SON.

The long-term mean OLR_{MJO}^2 for each season is shown in Figure 4. The maximum values in each season are located near longitude 120°E, consistent with animations of OLR_{MJO} , which contain eastward propagating disturbances that generally develop over Africa, intensify as they cross the Indian Ocean, reach maximum power near Micronesia, and then gradually decrease in strength crossing the Pacific Ocean. In a manner similar to the unfiltered OLR, the tropical region of maximum long-term mean OLR_{MJO}^2 shifts north and south with season, from near 10°S in DJF (Fig. 4a), to near the equator in MAM (Fig. 4b), to near 10°N in both JJA (Fig. 4c) and SON (Fig. 4d). In MAM and SON, the maximum exhibits a double-peaked structure, with the MAM maxima located just to the north and south of the equator, and the SON maxima located farther north, near 10°N and 20°N. The maximum values also vary with season, ranging from about 200 $W^2 m^{-4}$ in DJF down to about 80 $W^2 m^{-4}$ in JJA.

The longitudinal extent of significant OLR_{MJO}^2 varies with season. In DJF, the season with largest peak values, OLR_{MJO}^2 is most confined in longitude, with values along the tropical maximum reaching down to nearly 40 $W^2 m^{-4}$ over South America. In contrast, during JJA, when the maximum values are the lowest, OLR_{MJO}^2 in the tropical maximum is greater than 50 $W^2 m^{-4}$ at all longitudes, while in MAM, OLR_{MJO}^2 is greater than 60 $W^2 m^{-4}$ at all longitudes in a band just to the north of the equator.

Therefore, the MJO is locally the strongest during DJF, but is generally present over the greatest range of longitudes during MAM and JJA. This seasonal variation is consistent with

seasonal variations in the extent of tropical convection, as illustrated in the mean unfiltered OLR data (Figure 3). These data show that tropical convection is most confined in longitude during DJF when the ITCZ is nearly nonexistent, while during the other seasons tropical convection is prevalent over a broader range of longitudes in association with a stronger ITCZ across the Pacific. The results presented in Figure 4 are in agreement with previous studies of the seasonal cycle of OLR anomalies associated with the MJO (e.g. Weickman et al 1985; Madden 1986; Wang and Rui 1990).

b. Momentum flux convergence

The long-term mean of $\frac{-\partial u'v'}{\partial y}_{MJO}$ for each season is presented in Fig. 5. Overall, the basic patterns are similar for DJF (Fig. 5a), MAM (Fig. 5b), and SON (5d). In these seasons, the maximum values are located within 5° of the equator near longitude 120°E , where the long-term mean $\frac{-\partial u'v'}{\partial y}_{MJO}$ peaks at $4.3 \times 10^{-6} \text{ m s}^{-2}$ in DJF, at $3.8 \times 10^{-6} \text{ m s}^{-2}$ in MAM, and at $2.2 \times 10^{-6} \text{ m s}^{-2}$ in SON. The maxima in these three seasons are nearly collocated with the corresponding maxima in long-term mean OLR^2_{MJO} (see Fig. 4), and the maximum values are ranked similarly to the maximum OLR^2_{MJO} values for the respective three seasons. The results for DJF, MAM, and SON therefore suggest a close relationship between tropical convection associated with the MJO and upper tropical tropospheric momentum flux convergence at MJO wavenumbers and frequencies.

However, the results for JJA (Fig. 5c) differ considerably from the results for the other seasons. The biggest difference is in the location of the tropical extremes in $\frac{-\partial u'v'}{\partial y}_{MJO}$, as the

locations of the maximum and minimum values during JJA are nearly reversed from the other three seasons. In particular, the maximum JJA $\frac{-\partial u'v'}{\partial y}_{MJO}$, about $1.8 \times 10^{-6} \text{ m s}^{-2}$, is located in an equatorial band across South America and the Atlantic Ocean, while the minimum value is located near Micronesia. A couple of factors that likely contribute to the differences between JJA and the other seasons are the influence of the Indian and southeast Asian monsoons and the impact of increased convection off the west coast of Central America. The impact of the monsoons is suggested by the northward extension of momentum flux convergence into southeast Asia and the western Pacific Ocean, while the impact of convection off the coast of Central America is suggested by the maximum in $\frac{-\partial u'v'}{\partial y}_{MJO}$ beginning near this region and extending eastward.

The momentum flux convergence field for JJA (Fig. 5c) is further explored in Fig. 6, which separates $\frac{-\partial u'v'}{\partial y}_{MJO}$ into convergence and divergence components. Figure 6a was constructed by summing $\frac{-\partial u'v'}{\partial y}_{MJO}$ at each point over days on which $\frac{-\partial u'v'}{\partial y}_{MJO} > 0$ (convergence), and then dividing by 90, the total number of days in the season. Fig. 6b was similarly constructed considering days for which $\frac{-\partial u'v'}{\partial y}_{MJO} < 0$ (divergence). This separation leads to a better understanding of the total $\frac{-\partial u'v'}{\partial y}_{MJO}$ field for JJA by pointing out regions where momentum flux convergence (Fig. 6a) and divergence (Fig. 6b) are nearly offsetting and regions where one is dominant over the other.

Maximum convergence values occur in regions where disturbances at MJO wavenumbers and frequencies are strongest or most frequent or both. The average JJA tropical convergence (Fig. 6a) is greatest in a zonal band near 5°N. Within this band, the maximum values are located across South America extending into the Atlantic Ocean, likely in association with Central American convection (Fig. 3c). Also of note is the northward extension of relatively strong convergence over southeast Asia and the western Pacific Ocean in association with the monsoons, whereas average convergence at these more northern latitudes (e.g. 20°N) is much less at other longitudes.

The divergence field (Fig. 6b) suggests that the significant reduction in total $-\frac{\partial u'v'}{\partial y}_{MJO}$ during JJA in Micronesia relative to the other 3 seasons is related to the greater magnitude of momentum flux divergence around Micronesia and the Philippine Islands relative to that at similar latitudes over northern South America. The relatively strong divergence around Micronesia and the Philippine Islands is likely associated with the same disturbances responsible for the northward extension of convergence in association with the monsoons, while the relatively weak divergence across northern South America is due to relatively weak convergence at latitudes to the north and south. The combination of stronger convergence and weaker divergence over northern South America relative to the western Pacific Ocean is thus responsible for the reversal of the regions of maximum and minimum convergence during JJA relative to the other 3 seasons.

Finally, in contrast to the other three seasons, the JJA $-\frac{\partial u'v'}{\partial y}_{MJO}$ maximum (Fig. 5c) is not collocated with the JJA OLR_{MJO} maximum (Fig. 4c). Three points should be made regarding this discrepancy. First, longitudinal variability in both variables is much less during JJA than

during the other seasons, so collocation or lack thereof between the two peaks is not as significant as during the other seasons. Second, the peak in JJA $\frac{-\partial u'v'}{\partial y}_{MJO}$ does coincide with the general minimum in *unfiltered* OLR (Fig. 3c) that extends from off the west coast of South America across the Atlantic Ocean. This suggests that organized convection in this region, though not generally associated with the MJO, does produce momentum flux convergence at MJO frequencies and wavenumbers. Finally, the results presented in the remainder of this article show strong correlation between the two variables during JJA.

The results presented in this section suggest that tropical upper tropospheric momentum flux convergence at frequencies and wavenumbers associated with the MJO is related to disturbances in the OLR field with similar frequencies and wavenumbers. Furthermore, these disturbances in the OLR field are associated with enhanced tropical convection. Therefore, these results provide evidence that momentum flux convergence in the tropical upper troposphere is indeed related to tropical convection. Connections between MJO-related OLR anomalies and large-scale dynamics have been noted in a large number of previous studies (see Madden and Julian (1994) for references). However, to our knowledge the correlation between MJO-related OLR anomalies and upper tropospheric zonal momentum flux convergence has not previously been studied in detail. Such a study is the focus of the remainder of this paper.

5. Interannual correlation

In this section, the relationship between tropical convection and tropical upper tropospheric momentum flux convergence is explored by looking at the correlation between interannual variability in OLR_{MJO}^2 and $\frac{-\partial u'v'}{\partial y}_{MJO}$. High correlation between these quantities on

the interannual time scale would provide further evidence of a close connection between MJO-related disturbances in OLR and upper tropospheric momentum flux convergence.

The first step in calculating the interannual correlation is to construct seasonal mean fields (not shown) of OLR_{MJO}^2 and $\frac{-\partial u'v'}{\partial y}_{MJO}$ for each season and year in the 20 years under consideration. Then, for each season and at each gridpoint, 20-year time series of OLR_{MJO}^2 and $\frac{-\partial u'v'}{\partial y}_{MJO}$ are produced from these field. The ordinary Pearson correlation coefficient, r_{ia} , where “*ia*” denotes “interannual”, between these two time series is then calculated. Finally, the results at each gridpoint are compiled into maps of r_{ia} for each season. These maps, shown in Figure 7, reveal maximum correlation coefficients of 0.7 or greater during each season. Thus, since for data sets with 20 points (18 degrees of freedom), as considered here, correlation coefficients of 0.44 and greater are statistically significant at the 5% level, regions of significant correlation occur during each season. However, the locations, sizes, and maximum values of r_{ia} in, these regions vary significantly from season to season.

Overall, the greatest correlation coefficients are observed during DJF (Fig. 7a), when r_{ia} exceeds 0.4 in a band just south of the equator that stretches completely around the world. The region of greatest correlation, centered near Papua New Guinea where r_{ia} reaches 0.91, corresponds to the region of maximum OLR_{MJO}^2 (Fig. 4a) and $\frac{-\partial u'v'}{\partial y}_{MJO}$ (Fig. 5a) during DJF, while the reduced tropical correlations near South America correspond to a region where both quantities are much lower.

It should be kept in mind that large correlation coefficients, such as those just described, can be generated by a few well-placed data points that are significant outliers from the remaining

points, which may actually be poorly correlated. A useful statistic for testing if large correlations are produced by a few such data points is the rank correlation coefficient, $r_{ia,rank}$, which is calculated by first assigning ranks to the data points in each time series, and then calculating the ordinary correlation coefficient based on these ranks. In the 20-year time series considered here, a rank of 20 is assigned to the highest value, 19 to the second highest value, and so on, down to a rank of 1 for the lowest value. Large values of $r_{ia,rank}$ are produced when the rankings of the data points for the two time series are similar or, graphically, when a scatter plot of the two time series reveals a nearly monotonic increase in one variable with respect to the other, without regard to the actual values for the two data sets.

Figure 8a shows $r_{ia,rank}$ for DJF. In the tropics, $r_{ia,rank}$ is nearly as large as r_{ia} (Figure 7a), with the peak value reduced only to about 0.83. Since both $r_{ia,rank}$ and r_{ia} are high, we have great confidence that interannual variations in OLR_{MJO}^2 and $\frac{-\partial u'v'}{\partial y}_{MJO}$ are closely connected during DJF.

As in DJF, values of r_{ia} greater than 0.4 encircle the globe near the equator during MAM (Fig. 7b). Within this band, the region of maximum correlation is now located in the eastern Pacific Ocean, where r_{ia} peaks at 0.76. Therefore, unlike DJF, when the region of maximum correlation is collocated with the maxima in OLR_{MJO}^2 and $\frac{-\partial u'v'}{\partial y}_{MJO}$, the region of maximum correlation in MAM is located well to the east of these maxima. Also, starting in the western Atlantic Ocean and extending eastward across Africa and well into the Indian Ocean, the tropical maximum in r_{ia} is divided into three separate bands (centered near 5°N, 5°S, and 10°S) separated by bands of slightly lower correlation. Within these high correlation bands, r_{ia} is generally

greater than 0.5, and is greater than 0.6 in places. Thus, although the maximum value of r_{ia} is lower during MAM than DJF, significant values are found over a larger area during MAM.

The region of maximum $r_{ia,rank}$ for MAM (Fig. 8b) is located slightly to the west of the corresponding region in r_{ia} . This shift has placed the peak correlation region closer to, but still to the east of, the maxima in OLR_{MJO}^2 and $\frac{-\partial u'v'}{\partial y}_{MJO}$ for MAM. In addition, the peak value for $r_{ia,rank}$ of 0.71 is slightly less than the peak value for r_{ia} .

To help explain the differences between $r_{ia,rank}$ and r_{ia} for MAM, Figure 9 shows scatter plots of $\frac{-\partial u'v'}{\partial y}_{MJO}$ vs. OLR_{MJO}^2 for this season. Each point in these figures represents the MAM seasonal average for the indicated year and location. The scatter plot for $130^\circ\text{W}, 0^\circ$ (Fig. 9a), located within the region of maximum r_{ia} , reveals that the relatively large correlation coefficient at this location is largely a result of conditions in the years 1983, 1987, 1992, and especially 1998, as these years are outliers compared to the remaining years. Since these years are all El Niño years, it appears that the large correlation at this point in the eastern Pacific Ocean is related to the eastward shift in convection during El Niño. In the remaining years, $\frac{-\partial u'v'}{\partial y}_{MJO}$ and OLR_{MJO}^2 are relatively weak and there is no obvious relationship between the two quantities. For contrast, Fig. 9b shows the scatter plot at $110^\circ\text{E}, 0^\circ$, located near the equatorial minimum in r_{ia} . At this location, most of the data points show a more clear increase in $\frac{-\partial u'v'}{\partial y}_{MJO}$ with OLR_{MJO}^2 than at the previous point, leading to the higher rank correlation coefficient. In this case, r_{ia} is reduced by outlying years, in particular 1982, 1988, 1992, 1995, 1997, and 1998.

This is in contrast to the previous case, where the outlying years actually enhanced the correlation.

As in the two seasons already considered, a band of r_{ia} greater than 0.4 encircles the world just to the north of the equator during JJA (Fig. 7c), with another band of r_{ia} greater than 0.4 located to the south of the equator from the central Indian Ocean eastward to South America. In this season, maximum r_{ia} is located near 7.5°N across Africa, where the peak value is 0.76. The region of greatest r_{ia} during JJA is thus located between the widely separated JJA maxima in $-\frac{\partial u'v'}{\partial y}_{MJO}$ (Fig. 5c) and OLR_{MJO}^2 (Fig. 4c), being slightly closer to the former than to the latter.

This lack of coincidence in the location of maxima in these quantities is not a problem since, as mentioned in a previous section, longitudinal variability in the $-\frac{\partial u'v'}{\partial y}_{MJO}$ and OLR_{MJO}^2 fields during JJA is relatively weak. The general features in JJA $r_{ia,rank}$ (Fig. 8c) are similar to those for r_{ia} . Overall, the correlation between $-\frac{\partial u'v'}{\partial y}_{MJO}$ and OLR_{MJO}^2 during JJA is slightly less than in DJF or MAM, but is still significant over a large area in the deep tropics.

The SON maximum for both r_{ia} (Fig. 7d) and $r_{ia,rank}$ (Fig. 8d) is located in a narrow band across the Atlantic Ocean near 7.5°N , where the peak values of 0.75 and 0.71, respectively, are comparable to the corresponding peak values in MAM and JJA. However, the area covered by r_{ia} and $r_{ia,rank}$ greater than 0.4 is substantially less than during the other seasons. Therefore, the overall correlation between $-\frac{\partial u'v'}{\partial y}_{MJO}$ and OLR_{MJO}^2 during SON is substantially lower than during the other 3 seasons. On the other hand, there are still bands of positive correlation in the deep tropics that encircle most of the world.

The results presented in this section reveal a significant correlation between $\frac{-\partial u'v'}{\partial y}_{MJO}$ and OLR_{MJO}^2 on the interannual time scale during all seasons, providing additional evidence for the connection between tropical convection and tropical upper tropospheric momentum flux convergence. The largest correlation coefficients for any season are found during DJF, when the maximum r_{ia} reached 0.91. Although the maximum values for r_{ia} are lower during MAM and JJA, significant correlation is found over a larger area than during DJF. Finally, during SON the correlation is in general the lowest, although significant correlation is found in some, more limited, regions.

6. Daily correlation

In this section, the connection between $\frac{-\partial u'v'}{\partial y}_{MJO}$ and OLR_{MJO}^2 is further investigated by looking at the correlation between the two quantities on the daily time-scale. Correlation between these quantities on the daily time-scale is expected since, as can be seen in Figs. 1 and 2, OLR_{MJO} and $\frac{-\partial u'v'}{\partial y}_{MJO}$ are associated with discrete eastward-propagating disturbances that change position from day to day.

The correlation between OLR_{MJO}^2 and $\frac{-\partial u'v'}{\partial y}_{MJO}$ on the daily time-scale is examined using one-point correlation maps. The first step in constructing these maps, for a given season, is to combine the 90 daily maps of OLR_{MJO}^2 and $\frac{-\partial u'v'}{\partial y}_{MJO}$ for each of the 20 years considered into separate “time series” of 1800 maps for both variables. Note that there will be discontinuities between years in these time series. A one point correlation map is then produced

by calculating the daily correlation coefficients, r_{daily} , between the 1800-day time series of

$$\frac{-\partial u'v'}{\partial y}_{MJO}$$

at a selected “base point” and the corresponding time series of OLR_{MJO}^2 at all other

grid points. Such maps were produced for each season at $\frac{-\partial u'v'}{\partial y}_{MJO}$ base points in the deep

Tropics (10°N-10°S) separated by 30° longitude and 5° latitude, for a total of 60 base points for

each season. Overall, these maps reveal high correlation between day-to-day variability in

OLR_{MJO}^2 and $\frac{-\partial u'v'}{\partial y}_{MJO}$ in association with some base points during each season. Here, one-

point correlation maps are presented for several base points during each season to illustrate the

main findings of this portion of the study.

One-point correlation maps for DJF are shown in Fig. 10. Each panel in this figure

shows the correlation between the 1800-day time series of $\frac{-\partial u'v'}{\partial y}_{MJO}$ at the given base point and

the corresponding time series of OLR_{MJO}^2 at every grid point. The base point in Fig. 10a is

located at 5°S, 120°E. The one-point correlation coefficient in this case reaches 0.7 near Papua

New Guinea, located about 30° to the east of the base point. This is the greatest value of r_{daily}

reached in any of the one-point correlation maps examined in this study. Another peak, with

maximum r_{daily} of around 0.6, is observed over central Africa, about 100° to the west of the base

point. This general structure of a peak in r_{daily} to the east of the base point and a second peak

further to the west is present in most of the one-point correlation maps where significant r_{daily} is

observed, regardless of season. As will become clearer in the discussion of Figure 14 in Section

7, this structure is related to the dynamical response to tropical convective heating.

During DJF, peak r_{daily} values greater than 0.6 are observed to the east of the base point

for all base points at 5°S between longitudes 0° and 150°E. As the base point is moved east to

180° and into the eastern Pacific, the maximum r_{daily} decreases substantially. This is illustrated in Figs. 10b and c, in which the base point is located at 5°S, 180° and 5°S, 60°W, respectively. In Fig. 10b, r_{daily} exceeds 0.5 to the east of the base point, while in Fig. 10c the organized structure has largely disappeared and r_{daily} only reaches 0.2.

The general characteristics of the DJF one-point correlation maps for base points along the equator and along 10°S are similar to those for base points along 5°S just described, with r_{daily} of similar magnitude for base points along the equator and slightly lower for base points along 10°S. Therefore, for base points between the equator and 10°S in the Eastern Hemisphere during DJF, large positive values of r_{daily} are observed just to the east of the base point.

In contrast, negative r_{daily} is found in connection with DJF base points just north of the equator. For example, Fig. 10d shows the DJF one-point correlation with the $-\frac{\partial u'v'}{\partial y}_{MJO}$ base point at 10°N, 120°E, which is 15° to the north of the base point with maximum correlation (Fig. 10a). In this case, r_{daily} to the south of the base point is negative, with a minimum value of about -0.4. The negative values are likely indicative of the momentum flux *divergence* that is expected to the north and south of MJO-type disturbances.

One-point correlation maps for MAM are shown in Figure 11. In general, the results for MAM are similar to those for DJF, with the largest values of r_{daily} again found in association with base points at and slightly south of the equator in the Eastern Hemisphere. Fig. 11a shows the one-point correlation with the $-\frac{\partial u'v'}{\partial y}_{MJO}$ base point at 0°, 90°E. This base point is near the middle of the range of longitudes, 60E°-120°E, for which the base points are associated with maximum r_{daily} of about 0.5. Within this range, maxima in r_{daily} are found both to the southeast and to the southwest of the base points. Figure 11b shows the correlation with a base point

further to the east at 0° , 180° , with which the maximum r_{daily} has decreased somewhat to 0.4 slightly to the east of the base point. Figure 11c shows the correlation with a base point still further to the east at 0° , 60°W . The maximum r_{daily} associated with this base point is somewhat lower, but is still greater than 0.3. Thus, the difference between the maximum r_{daily} associated with base points around 120°E and that associated with base points in the eastern Pacific Ocean is significantly less during MAM than during DJF. This finding is in agreement with other results presented in this article showing that a number of variables have their highest annual values during DJF, but that large values are more confined to the region around Micronesia during DJF than during the other seasons. Finally, Fig. 11d shows the one-point correlation with the $\frac{-\partial u'v'}{\partial y}_{MJO}$ base point at 10°N , 90°E . As was the case in DJF, negative r_{daily} is observed to the south of this base point located north of the equator, again likely due to momentum flux divergence associated with MJO-related disturbances.

The one-point correlation maps for JJA (Fig. 12) differ substantially from those for DJF and MAM, as expected based on the seasonal differences found in other variables elsewhere in this article. During JJA, the largest values of r_{daily} are now associated with $\frac{-\partial u'v'}{\partial y}_{MJO}$ base points to the north of the equator, with large values of r_{daily} observed over the greatest range of longitudes in association with base points at 5°N . Figure 12a shows r_{daily} associated with the base point at 5°N , 60°W . Values of r_{daily} exceed 0.6 about 30° to the east of this base point, with another maximum in r_{daily} of 0.4 located about 150° to the west. As shown in Fig. 12b for the base point at 5°N , 120°E , this basic structure at 5°N shows little longitudinal variability, as maximum r_{daily} values in excess of 0.5 are found in association with base points at all longitudes except for 60°E , and even there the maximum r_{daily} exceeds 0.4.

In contrast to the situation at 5°N, r_{daily} at 10°N exhibits greater sensitivity to the longitude of the base point. The JJA r_{daily} maps for base points from 60°W to 0° at 10°N (not shown) are very similar to that for the base point at 5°N, 60°W (Fig. 12a), with maximum r_{daily} values exceeding 0.6. However, the maximum r_{daily} values associated with base points outside of this longitude range are significantly lower, as illustrated in Fig. 12c for the base point at 10°N, 150°E. Lastly, Fig. 12d shows r_{daily} with the base point at 10°S, 60°W. Once again, negative values for r_{daily} are observed in association with base points located in the opposite hemisphere from the strongest convection.

Finally, one-point correlation maps for SON are shown in Figure 13. Overall, the results are similar to those for JJA, although the maximum values for r_{daily} are slightly lower. As in JJA, the largest values for r_{daily} are found in association with base points at 5°N. This is illustrated in Figs. 13a,b, and c, which show r_{daily} associated with base points located at 5°N, 0°; 5°N, 90°E; and 5°N, 180°, respectively. Maximum values for r_{daily} of around 0.4 are observed slightly to the east of each of these base points. Another maximum in r_{daily} is also observed further to west in each case, and this western maximum is especially strong in Fig. 13c, where the peak r_{daily} is about the same as in the eastern peak. The maximum r_{daily} associated with base points further to the east along 5°N is slightly lower, but still remains above 0.3 for all base points. Lastly, Fig. 13d shows r_{daily} with the base point near 10°S, 150°E, and once again negative r_{daily} is associated with base points in the opposite hemisphere from the strongest convection.

The one-point correlation maps presented in this section reveal a strong correlation between $\frac{-\partial u'v'}{\partial y}_{MJO}$ and OLR^2_{MJO} on the daily time scale during all seasons. The correlation is generally strongest for base points located at latitudes where convection is most prevalent and where the MJO exhibits the strongest signal. The results presented in this section, combined

with the results presented in the preceding sections, provide strong evidence of a close connection between tropical convection and tropical upper tropospheric momentum flux convergence.

7. Summary and discussion

The connection between tropical convection and tropical upper tropospheric momentum flux convergence, an important component of the Boehm and Lee (2003) hypothesis, has been investigated in this paper. This has been accomplished by studying the correlation between outgoing longwave radiation data produced by the NOAA CIRES Climate Diagnostics Center, used here as a proxy for tropical convection, and momentum flux convergence at 150 mb calculated from NCEP-NCAR reanalysis u and v data. Based on results presented in Lee (1999) showing that a large portion of tropical upper tropospheric momentum flux convergence occurs at MJO scales, both data sets have been filtered to isolate variability associated with disturbances at MJO frequencies and wavenumbers.

Visual comparison of daily and long-term mean maps of OLR_{MJO}^2 and $\frac{-\partial u'v'}{\partial y}_{MJO}$ suggests that these two quantities are closely related. This relationship is quantified by calculating correlation coefficients between time series of the two quantities on both the annual and daily time scales. These calculations show that the two quantities are indeed highly correlated and that the strength of the correlation and regions covered by significant correlation vary from season to season.

Overall the largest correlation coefficients, both on the annual and daily time scales, are obtained during DJF. However, greater longitudinal variability in the strength of the correlation occurs in DJF than in the other three seasons, with very strong correlation in a region centered in

the tropical western Pacific, but much weaker correlation near South America. During the other three seasons, the correlation coefficients, especially those for the daily time scale, vary less with longitude. This difference is related to the general confinement of organized convection to the region around Micronesia during DJF in contrast to the other seasons when organized convection has greater longitudinal extent in association with the ITCZ and Asian monsoon.

For all seasons, significant correlations are generally found in bands with limited latitudinal extent. These bands move north and south with season, following the changing latitude of the most significant convection and the sun. Thus, significant correlation is found primarily to the south of the equator during DJF, near the equator during MAM, and to the north of the equator during JJA and SON.

According to the hypothesis presented by Boehm and Lee (2003), momentum flux convergence in the tropical upper troposphere is caused by waves generated by tropical convection, and the results of this study support this statement. However, significant correlation between OLR_{MJO}^2 and $\frac{-\partial u'v'}{\partial y}_{MJO}$ does not by itself imply a causal relationship between the two quantities, and additional facts are needed to support the conclusion that organized tropical convection is responsible for tropical upper tropospheric momentum flux convergence.

One such fact is the finding that upper tropospheric momentum flux *convergence*, rather than momentum flux *divergence*, is closely correlated with disturbances in OLR. According to Held (1975), meridional *convergence* of zonal wave momentum flux is generally expected into the latitude of a wave source, while meridional *divergence* of zonal wave momentum flux is expected at latitudes away from the source region (see Boehm and Lee (2003) for additional discussion). Therefore, the presence of convergence at the same latitudes where MJO-related disturbances are most prevalent shows that the waves responsible for the convergence are

generated at these latitudes, and organized tropical convection associated with the MJO is the most likely wave source in the deep Tropics.

Further support for the conclusion that tropical convection is responsible for tropical upper tropospheric momentum flux convergence is found in the one-point correlation maps (Figures 10-13) used to examine the daily correlation between OLR_{MJO}^2 and $\frac{-\partial u'v'}{\partial y}_{MJO}$. These maps provide information on the structure of disturbances in the OLR as well as on the relationship between momentum flux convergence and these large-scale disturbances. In particular, maps containing significant correlation values (e.g. Fig. 10a) reveal that MJO-filtered upper tropical tropospheric momentum flux convergence is most highly correlated with disturbances in the MJO-filtered OLR field centered about 30° longitude to the east of the base point and also on the order of 100° longitude to the west of the base point. This structure brings to mind the dynamical response to idealized tropical heating, in which tropical waves propagate both to the east and west away from the heat source (Gill 1980; Yamagata and Hayashi 1984; Salby and Garcia 1987; Sardeshmukh and Hoskins 1988).

The relationship between the results presented in this paper and previous work on the atmospheric response to tropical heating becomes much clearer if one-point correlation maps are produced in which the roles of $\frac{-\partial u'v'}{\partial y}_{MJO}$ and OLR_{MJO}^2 are reversed from their roles in Figures 10-13. In these new one-point correlation maps, the correlation is calculated between the time-series of $\frac{-\partial u'v'}{\partial y}_{MJO}$ at every gridpoint and the time-series of OLR_{MJO}^2 at a given base point. Four such one-point correlation maps are shown in Figure 14, one for each season.

The one-point correlation map for DJF with the OLR_{MJO}^2 base point at 5°S, 120°E, the same location as the $\frac{-\partial u'v'}{\partial y}_{MJO}$ base point in Fig. 10a, is shown in Fig. 14a. The most striking feature in this figure is the region of high correlation that extends from about 80° west of to about 20° east of the base point. Within this region, the correlation coefficient peaks at slightly more than 0.7 about 20° west of the base point. This region has a “half-butterfly” shape, with a weak axis of slightly lower correlation extending westward from the center, and axes of slightly higher correlation extending both to the northwest and southwest from the center. Moving east from the base point, the correlation rapidly declines to near 0.1 about 40° to the east of the base point, and then increases somewhat to a peak of slightly more than 0.3 about 90° to the east of the base point.

The correlation pattern shown in Fig. 14a is very similar to Figure 1b in Gill (1980), which shows the theoretical pressure perturbation response to a region of heating symmetric about the equator. Both figures exhibit a double-lobe structure to the west of the convection (represented by the base point in Fig. 14a, and the heating region in Gill (1980)) and a single lobe extending to the east. The double-lobe pattern to the west and single-lobe pattern to the east are caused, respectively, by mixed Rossby-gravity waves propagating westward from the convection and Kelvin waves propagating eastward from the convection (Salby and Garcia 1987; Gill 1980).

Therefore, it appears that a large portion of the momentum flux convergence in the tropical upper troposphere is associated with tropical waves, in particular mixed Rossby-gravity waves. The greater contribution of mixed Rossby-gravity waves than Kelvin waves to momentum flux convergence is expected for two reasons. First, the structure of mixed Rossby-gravity waves is better suited for the meridional transport of zonal momentum than that of Kelvin

waves, since the wind fields associated with the former have a meridional component, whereas those for the latter do not (compare Andrews (1987) Fig. 22 and Fig. 20). Second, Kelvin waves travel 3 times faster than mixed Rossby-gravity waves (Gill 1980), so any momentum flux convergence that is generated by Kelvin waves would be more spread out spatially, thus likely reducing the correlation at a given location.

Regions of negative correlation are found in Fig. 14a both to the north and south of the deep tropical band of positive correlation just described. This negative correlation is most likely a signature of momentum flux divergence associated with the same waves responsible for producing the momentum flux convergence and positive correlation in the deep tropics.

Although Fig. 14a shows a one-point correlation map that includes about the largest correlation coefficients for any season and base point location looked at, significant correlation coefficients and similar correlation structures are observed in association with DJF base points over an area similar to that for which significant DJF one-point correlations with $\frac{-\partial u'v'}{\partial y}_{MJO}$ base points were found in Section 6. In addition, significant correlation coefficients and similar correlation structures are observed in association with base points during the other seasons, as illustrated by one example for each season in Figs. 14b-d for MAM, JJA, and SON, respectively. As in DJF, the base points with which significant correlation is found during the other seasons are located over regions similar to those for which significant one-point correlations were found in Section 6.

According to the mechanism presented by Boehm and Lee (2003), rising motion is generated in the upper troposphere of the deep Tropics in response to the meridional convergence of zonal momentum flux in this region. Our results show that this momentum flux convergence is not zonally symmetric, as modeled by Boehm and Lee (2003), but rather occurs

intermittently in eastward-propagating regions located primarily to the west of the region of convection associated with the MJO. Therefore, we hypothesize that the rising motion in the tropopause transition layer associated with the Boehm and Lee (2003) mechanism similarly occurs intermittently over limited regions, primarily to the west of the region of convection associated with the MJO. In addition, since the momentum flux convergence is confined to a relatively small region and will therefore be stronger, the rising motion in these regions is expected to be stronger than that calculated by Boehm and Lee (2003). A more complete modeling study of this mechanism would include forcing a three-dimensional dynamical model with spatially and temporally varying fields of momentum flux convergence, such as those presented in Figure 2.

Finally, our results have implications to moisture transport in the tropopause transition layer (TTL) and the formation of thin cirrus layers near the tropical tropopause. Although, convection associated with the MJO transports huge quantities of moisture into the tropical upper troposphere, recent work suggests that tropical convective detrainment is largely capped near the base of the TTL (e.g. Gettelman et al. 2002; Folkins et al. 1999; Highwood and Hoskins 1998). We suggest that as the MJO related convection moves to the east, the water vapor left behind is transported vertically through the depth of the TTL by rising motion generated by the Boehm and Lee (2003) mechanism. As the water vapor ascends to near the cold-point tropopause, thin cirrus may form. As the rate of ascent that might be generated by the Boehm and Lee (2003) mechanism in localized regions is not known, it is unclear whether or not this ascent would be sufficient to form cirrus. However, as shown by Boehm and Verlinde (2000) for the case of Kelvin waves, the rate of ascent and associated with tropical waves near the tropopause is sometimes sufficient for cirrus formation.

Acknowledgments

This research was performed while MTB held a National Research Council Research Associateship Award at the NASA Goddard Space Flight Center. Both the interpolated OLR data and the NCEP Reanalysis data were provided by the NOAA-CIRES Climate Diagnostics Center, Boulder, Colorado, USA, from their Web site at <http://www.cdc.noaa.gov/>. We gratefully acknowledge Sukyoung Lee for her suggestion to calculate the momentum flux convergence in grid-point space and Scott Curtis for his comments on an earlier manuscript.

References

- Andrews, D. G., J. R. Holton, and C. B. Leovy, 1987: *Middle Atmospheric Dynamics*. Academic Press, 489 pp.
- Boehm, M. T., and S. Lee, 2003: The implications of tropical Rossby waves for tropical tropopause cirrus formation and for the equatorial upwelling of the Brewer-Dobson circulation. *J. Atmos. Sci.*, **60**, 247-261.
- Boehm, M. T., and J. Verlinde, 2000: Stratospheric influence on upper tropospheric tropical cirrus. *Geophys. Res. Lett.*, **27**, 3209-3212.
- Chen, T.-C., 1985: On the time-variation in the tropical energetics of large-scale motions during the FGGE Summer. *Tellus*, **37**, 258-275.
- Folkens, I., M. Loewenstein, J. Podolske, S. J. Oltmans, and M. Proffitt, 1999: A barrier to vertical mixing at 14 km in the Tropics: Evidence from ozonesondes and aircraft measurements. *J. Geophys. Res.*, **104**, 22,095-22,102.
- Gettelman, A., M. L. Salby, and F. Sassi, 2002: Distribution and influence of convection in the tropical tropopause region. *J. Geophys. Res.*, **107** (D10), 4080, doi:10.1029/2001JD001048.
- Gill, A. E., 1980: Some simple solutions for the heat-induced tropical circulation. *Quart. J. Roy. Meteor. Soc.*, **106**, 447-462.
- Gruber, A., 1974: Wavenumber-frequency spectra of satellite-measured brightness in the tropics. *J. Atmos. Sci.*, **31**, 1675-1680.
- Gruber, A., and A. F. Krueger, 1984: The status of the NOAA outgoing longwave radiation dataset. *Bull. Amer. Meteor. Soc.*, **65**, 1675-1680.

- Gu, G., and C. Zhang, 2001: A spectrum analysis of synoptic-scale disturbances in the ITCZ. *J. Climate*, **14**, 2725-2739.
- Held, I. M., 1975: Momentum transport by quasi-geostrophic eddies. *J. Atmos. Sci.*, **32**, 1494-1497.
- Hendon, H. H., and B. Liebmann, 1991: The structure and annual variation of antisymmetric fluctuation of tropical convection and their association with Rossby-gravity waves. *J. Atmos. Sci.*, **48**, 2127-2140.
- Highwood, E. J., and B. J. Hoskins, 1998: The tropical tropopause. *Quart. J. Roy. Meteor. Soc.*, **124**, 1579-1604.
- Lee, S., 1999: Why are the climatological zonal winds easterly in the equatorial upper troposphere? *J. Atmos. Sci.*, **56**, 1353-1363.
- Madden, R. A., 1986: Seasonal variations of the 40-50 day oscillation in the Tropics. *J. Atmos. Sci.*, **43**, 3138-3158.
- Madden, R. A., and P. R. Julian, 1971: Detection of a 40-50 day oscillation in the zonal wind in the tropical Pacific. *J. Atmos. Sci.*, **28**, 702-708.
- Madden, R. A., and P. R. Julian, 1972: Description of global-scale circulation cells in the Tropics with a 40-50 day period. *J. Atmos. Sci.*, **29**, 1109-1123.
- Salby, M. L., R. R. Garcia, 1987: Transient response to localized episodic heating in the Tropics. Part I: Excitation and short-time near-field behavior. *J. Atmos. Sci.*, **44**, 458-498.
- Sardeshmukh, P. D., and B. J. Hoskins, 1988: The generation of global rotational flow by steady idealized tropical divergence. *J. Atmos. Sci.*, **45**, 1228-1251.
- Wang, B., and H. Rui, 1990: Synoptic climatology of transient tropical intraseasonal convection anomalies: 1975-1985. *Meteorol. Atmos. Phys.* **44**, 43-61.

Weickmann, K. M., G. R. Lussky, and J. E. Kutzbach, 1985: Intraseasonal (30-60 day)

fluctuations of outgoing longwave radiation and 250 mb streamfunction during northern winter. *Mon. Wea. Rev.*, **113**, 941-961.

Wheeler, M., and G.N. Kiladis, 1999: Convectively coupled equatorial waves: Analysis of

clouds and temperature in the wavenumber-frequency domain. *J. Atmos. Sci.*, **56**, 374-399.

Yamagata, T., and Y. Hayashi, 1984: A simple diagnostic model for the 30-50 day oscillation in

the Tropics. *J. Meteor. Soc. Japan*, **62**, 709-717.

Figure Captions

Figure 1. NOAA OLR data filtered to isolate variability on MJO scales. See text for details of the filtering applied. The maps shown in (a)-(d) show OLR_{MJO} on four days spaced 15 days apart: (a) 30 Dec. 1989, (b) 14 Jan. 1990, (c) 29 Jan. 1990, and (d) 13 Feb. 1990. (e) Longitude-time plot of OLR_{MJO} at latitude 5°S for DJF 1989-90, which includes the days shown in (a)-(d). The contour interval in each panel is 5 W m^{-2} , and negative contours are dotted.

Figure 2. The meridional convergence of zonal momentum flux calculated from NCEP-NCAR reanalysis u and v data that has been filtered to isolate variability on MJO scales. See text for

calculation details. Shown are maps of $\frac{-\partial u'v'}{\partial y}_{MJO}$ for: (a) 30 Dec. 1989, (b) 14 Jan. 1990, (c) 29

Jan. 1990, and (d) 13 Feb. 1990. (e) Longitude-time plot of $\frac{-\partial u'v'}{\partial y}_{MJO}$ at latitude 5°S for DJF

1989-90, which includes the days shown in (a)-(d). The contour interval in each panel is $5 \times 10^{-6} \text{ m s}^{-2}$, and negative contours are dotted.

Figure 3. Long-term (20-year) seasonal means of NOAA OLR data for (a) DJF, (b) MAM, (c) JJA, and (d) SON. Contour interval is 10 W m^{-2} .

Figure 4. Long-term (20-year) seasonal means of MJO-filtered OLR power, OLR_{MJO}^2 , for (a) DJF, (b) MAM, (c) JJA, and (d) SON. Contour interval is 10 W m^{-2} .

Figure 5. Long-term (20-year) seasonal means of MJO-filtered momentum flux convergence, $\frac{-\partial u'v'}{\partial y}_{MJO}$, for (a) DJF, (b) MAM, (c) JJA, and (d) SON. The contour interval is $5 \times 10^{-7} \text{ m s}^{-2}$ and negative contours are dotted.

Figure 6. (a) Convergence, and (b) divergence, components of the total MJO-filtered momentum flux convergence, $\frac{-\partial u'v'}{\partial y}_{MJO}$, for JJA (see Fig. 5c). The contour interval is $2 \times 10^{-7} \text{ m s}^{-2}$ and negative contours are dotted.

Figure 7. Correlation coefficient, r_{ia} , between 20-year time series of seasonal average

$\frac{-\partial u'v'}{\partial y}_{MJO}$ and OLR_{MJO}^2 at each grid point for (a) DJF, (b) MAM, (c) JJA, and (d) SON. The

contour interval is 0.1, negative contours are dotted, and contours are not plotted for -0.1, 0.0, or 0.1. Values between 0.4 and 0.6 are lightly shaded, while values greater than 0.6 are darkly shaded.

Figure 8. Similar to Figure 7, but the rank correlation coefficient, $r_{ia,rank}$ is plotted instead of r_{ia} .

Figure 9. Scatter plots of seasonal mean $\frac{-\partial u'v'}{\partial y}_{MJO}$ vs. seasonal mean OLR_{MJO}^2 for MAM. The plots shown are for the locations: (a) $0^\circ, 130^\circ\text{W}$ and (b) $0^\circ, 110^\circ\text{E}$. Each point is labeled with its corresponding year.

Figure 10. One-point correlation maps for DJF showing the correlation coefficient between the 20-year time series of daily DJF $\frac{-\partial u'v'}{\partial y}_{MJO}$ at a given base point and the 20-year time series of DJF OLR_{MJO}^2 at every point. The base points are indicated with an "X" and are located at: (a) $5^\circ\text{S}, 120^\circ\text{E}$, (b) $5^\circ\text{S}, 180^\circ$, (c) $5^\circ\text{S}, 60^\circ\text{W}$, and (d) $10^\circ\text{N}, 120^\circ\text{E}$. The contour interval is 0.1 and negative contours are dotted.

Figure 11. Same as Figure 10, except season is MAM and base points are located at: (a) $0^\circ, 90^\circ\text{E}$, (b) $0^\circ, 180^\circ$, (c) $0^\circ, 60^\circ\text{W}$, and (d) $10^\circ\text{N}, 90^\circ\text{E}$.

Figure 12. Same as Figure 10, except season is JJA and base points are located at: (a) $5^\circ\text{N}, 60^\circ\text{W}$, (b) $5^\circ\text{N}, 120^\circ\text{E}$, (c) $10^\circ\text{N}, 150^\circ\text{E}$, and (d) $10^\circ\text{S}, 60^\circ\text{W}$.

Figure 13. Same as Figure 10, except season is SON and base points are located at: (a) $5^\circ\text{N}, 0^\circ$, (b) $5^\circ\text{N}, 90^\circ\text{E}$, (c) $5^\circ\text{N}, 180^\circ$, and (d) $10^\circ\text{S}, 150^\circ\text{E}$.

Figure 14. One-point correlation maps calculated with the roles of $\frac{-\partial u'v'}{\partial y}_{MJO}$ and OLR_{MJO}^2

reversed from their roles in Figs. 10-13. These maps show the correlation coefficients between the 20-year time series of daily OLR_{MJO}^2 during the given season at the given base point and the

20-year time series $\frac{-\partial u'v'}{\partial y}_{MJO}$ for the given season at every point. The base points are indicated

with an "X" and are for the seasons and base point locations given by: (a) DJF at 5°S,120°E, (b)

MAM at 10°S,120°E, (c) JJA at 5°N,60°W, and (d) SON at 10°N,180°. The contour interval is

0.1 and negative contours are dotted.

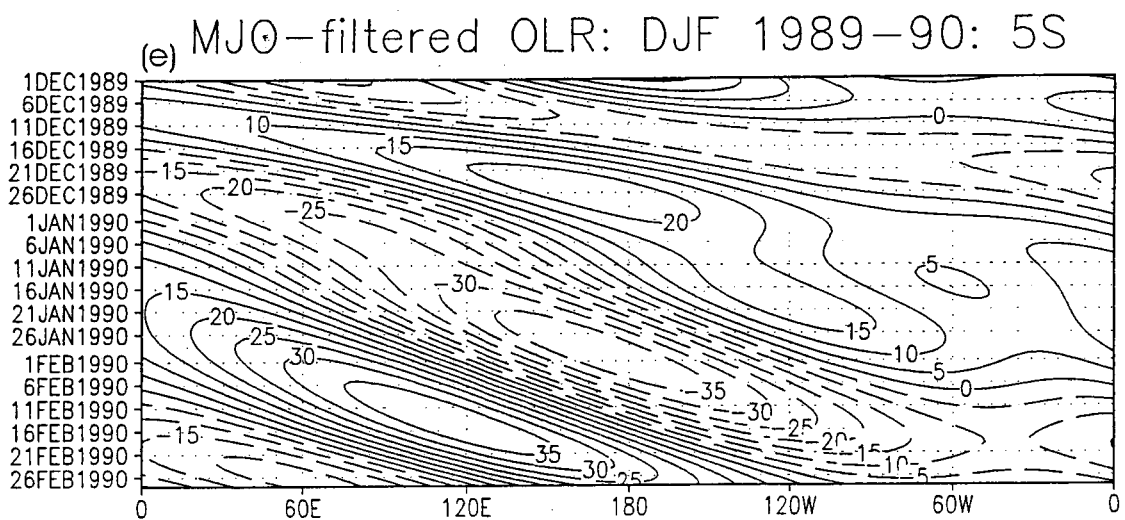
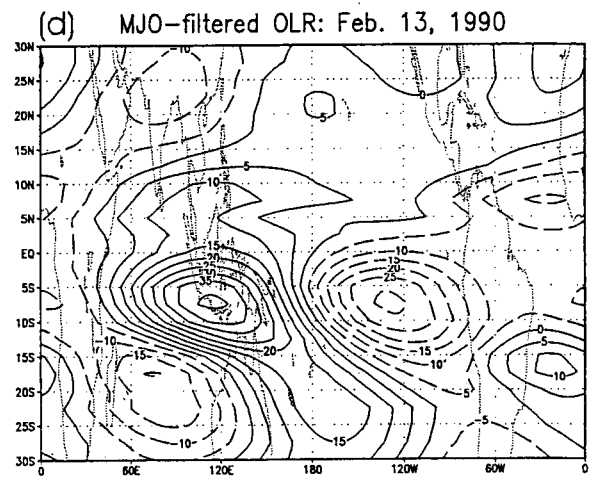
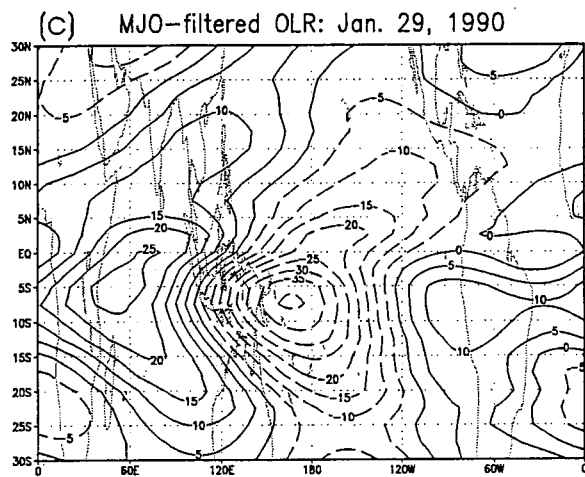
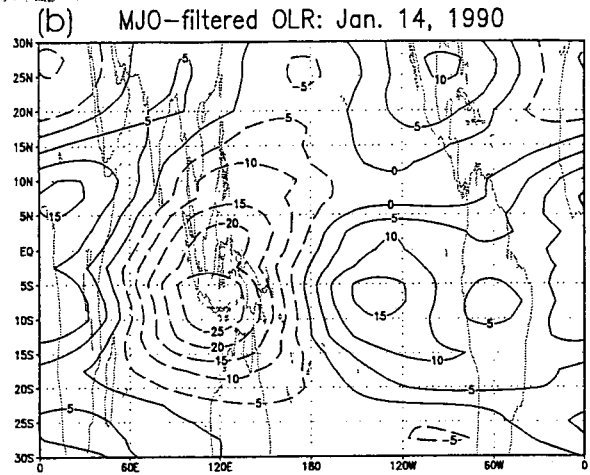
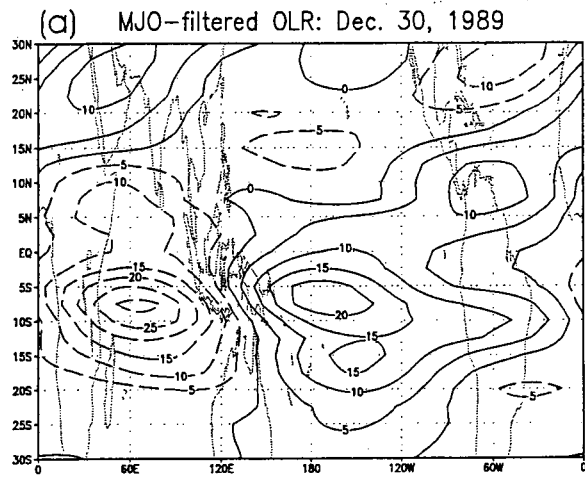
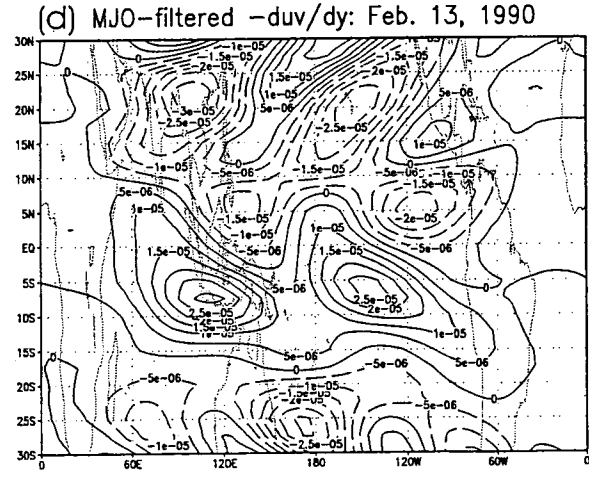
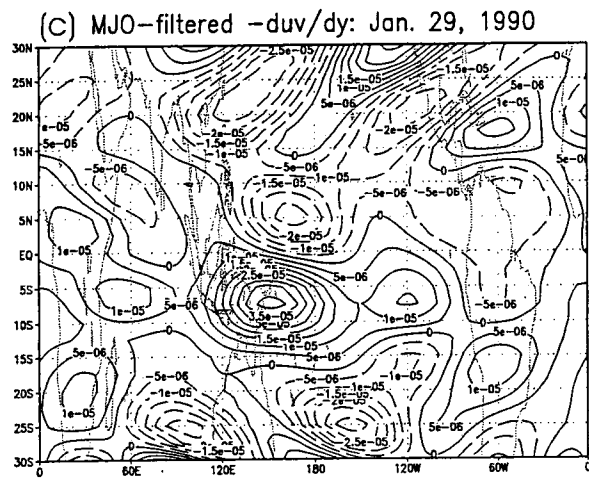
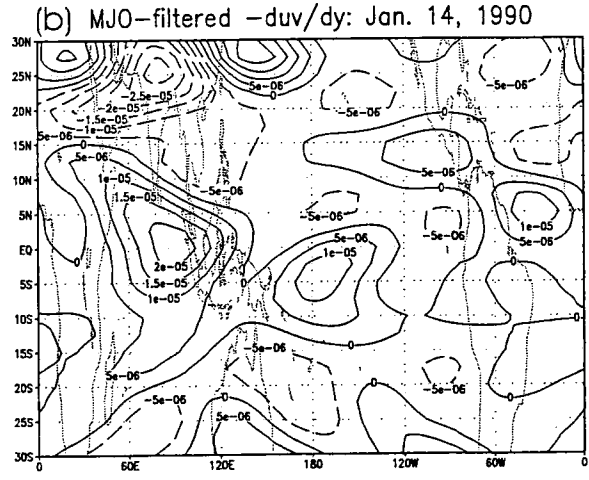
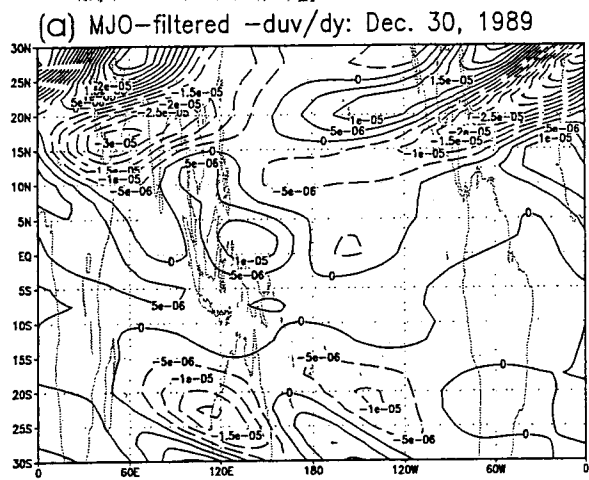


Figure 1



(e) MJO-filtered $-\text{div}/\text{dy}$: DJF 1989-90: 5S

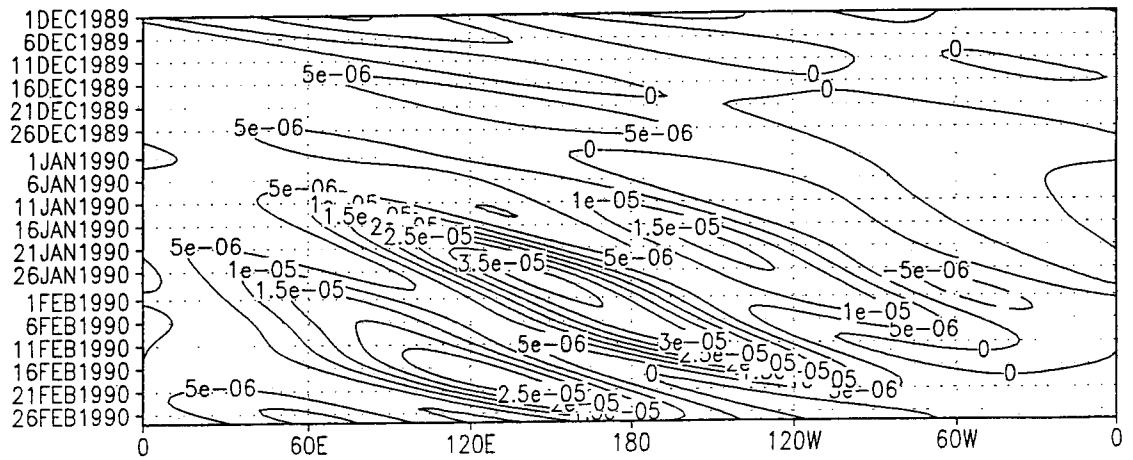
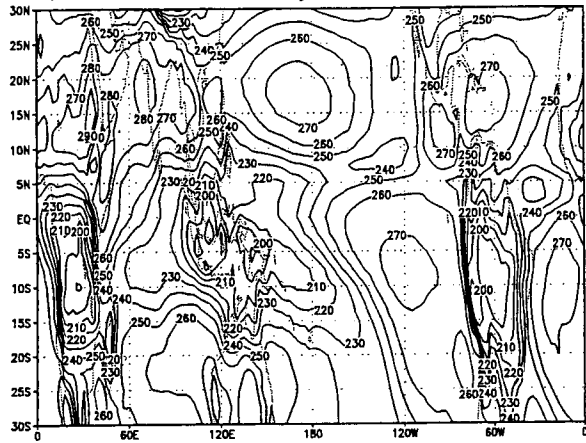
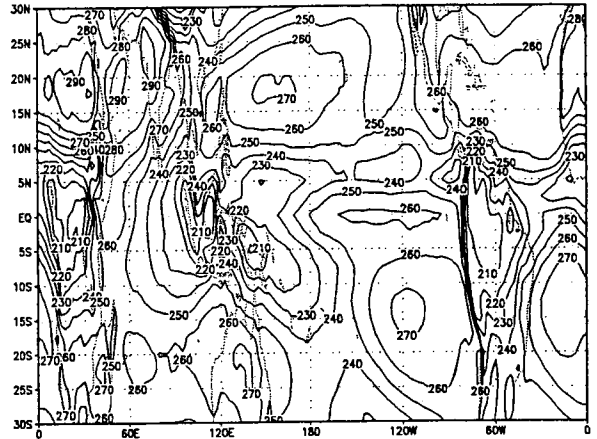


Figure 2

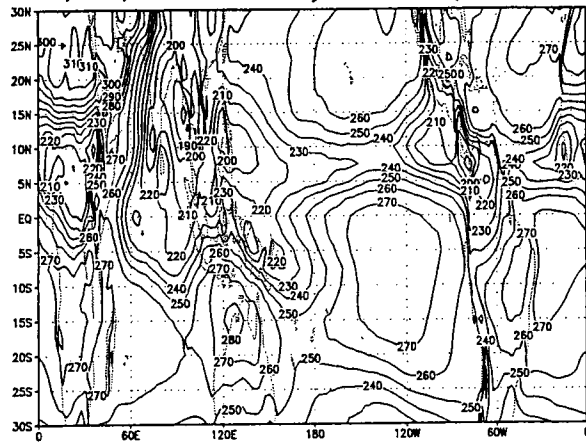
(a)
OLR, DJF, unfiltered: 20 year mean (J1983-J2002)



(b)
OLR, MAM, unfiltered: 20 year mean (1983-2002)



(c)
OLR, JJA, unfiltered: 20 year mean (1983-2002)



(d)
OLR, SON, unfiltered: 20 year mean (1983-2002)

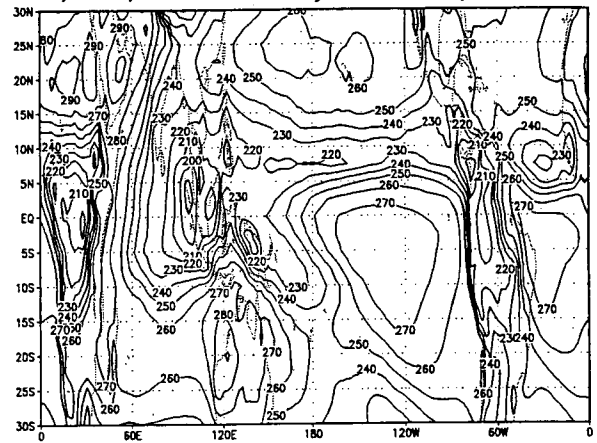
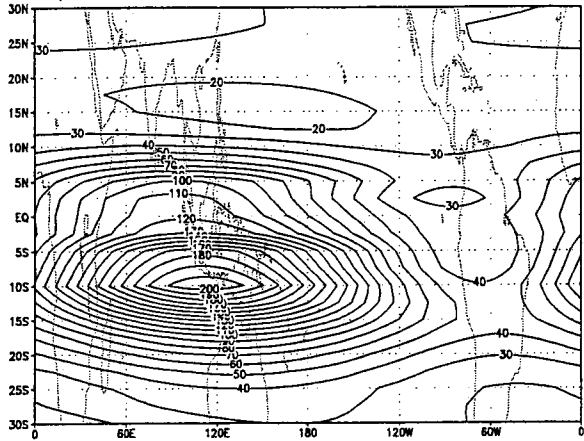
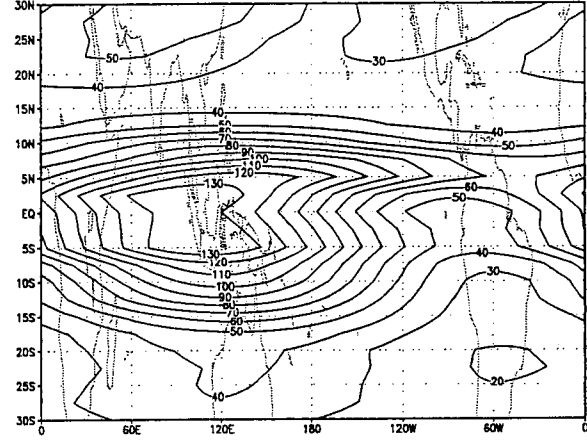


Figure 3

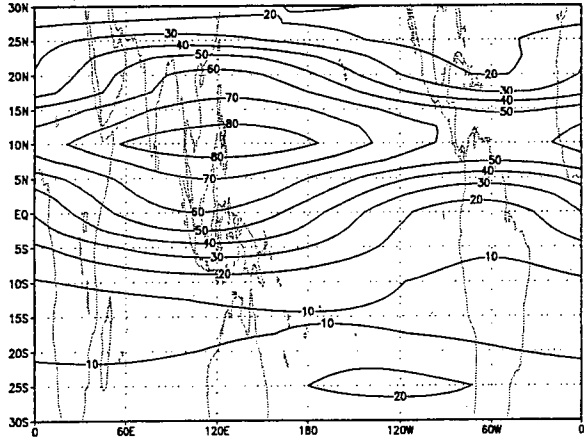
(a)
OLR power, DJF, MJO: 20year mean (J1983-J2002)



(b)
OLR power, MAM, MJO: 20year mean (1983-2002)



(c)
OLR power, JJA, MJO: 20year mean (1983-2002)



(d)
OLR power, SON, MJO: 20year mean (1983-2002)

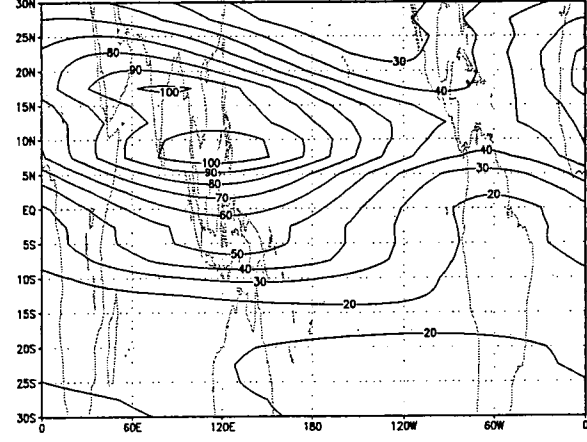
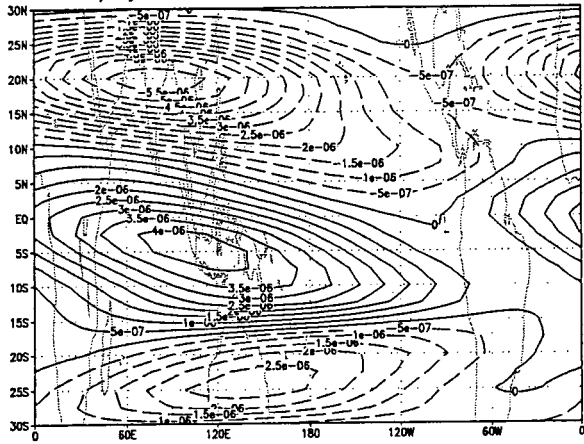
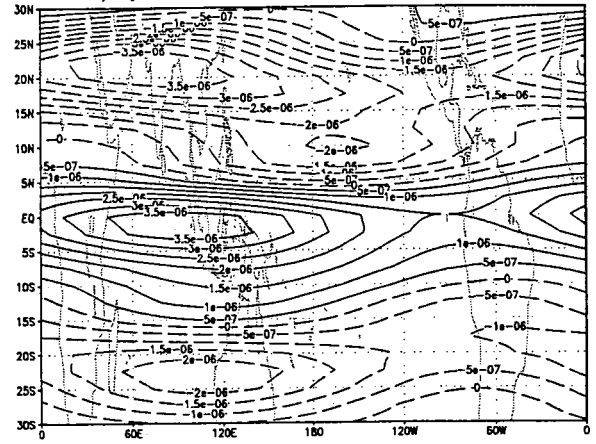


Figure 4

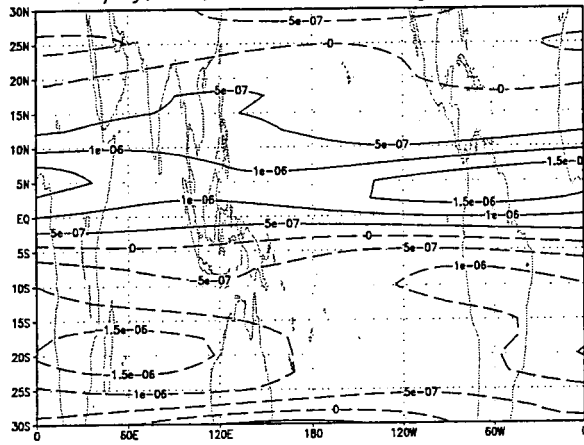
(a)
-div/dy, DJF, MJO filtered: long-term mean



(b)
-div/dy, MAM, MJO filtered: long-term mean



(c)
-div/dy, JJA, MJO filtered: long-term mean



(d)
-div/dy, SON, MJO filtered: long-term mean

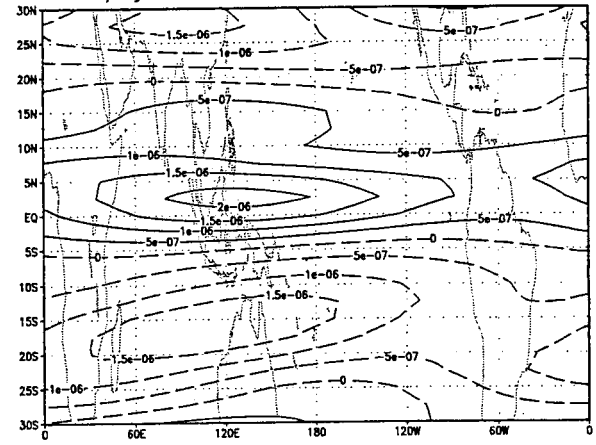
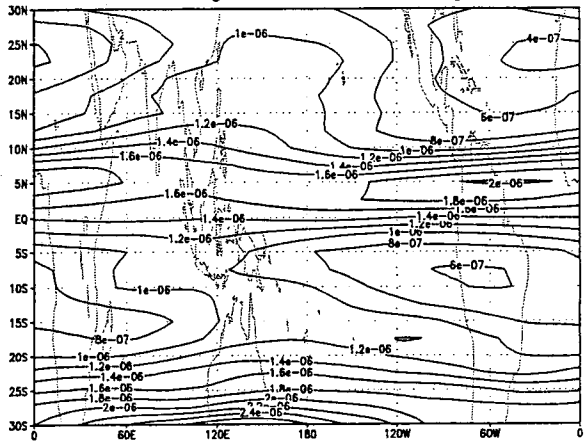


Figure 5

(a)
mom. flux convergence, JJA, MJO, long-term mean



(b)
mom. flux divergence, JJA, MJO, long-term mean

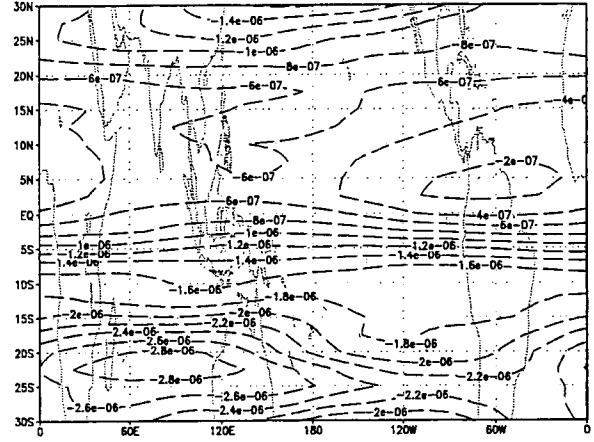
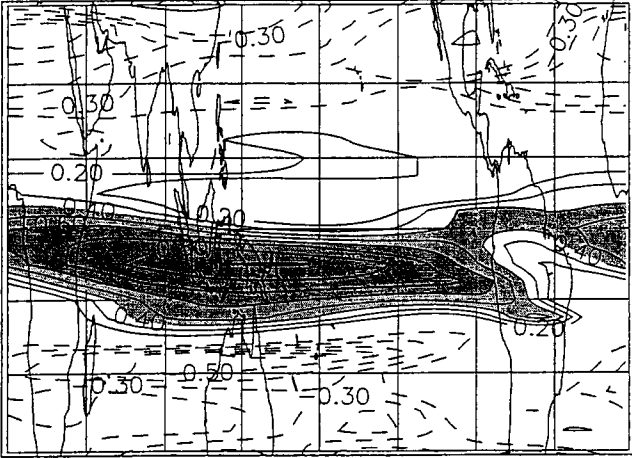
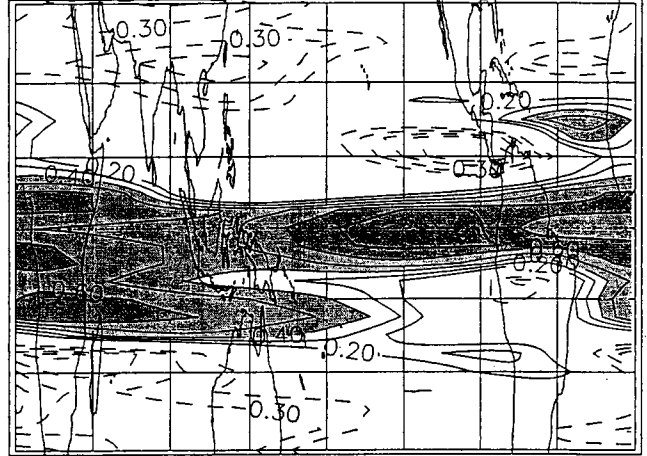


Figure 6

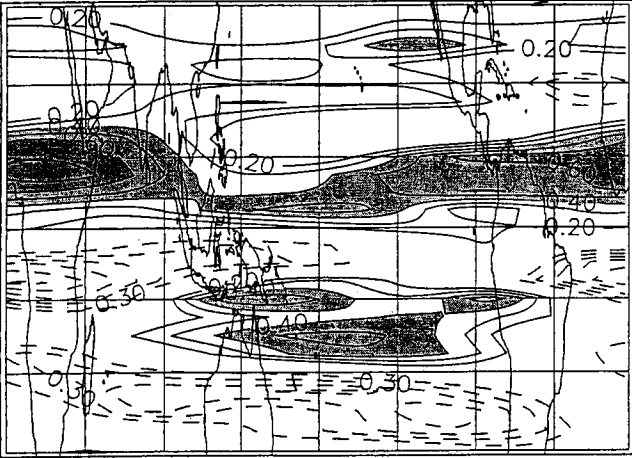
(a) inter-annual correlation: MJO filtered DJF OLR power and $-duv/dy$



(b) inter-annual correlation: MJO filtered MAM OLR power and $-duv/dy$



(c) inter-annual correlation: MJO filtered JJA OLR power and $-duv/dy$



(d) inter-annual correlation: MJO filtered SON OLR power and $-duv/dy$

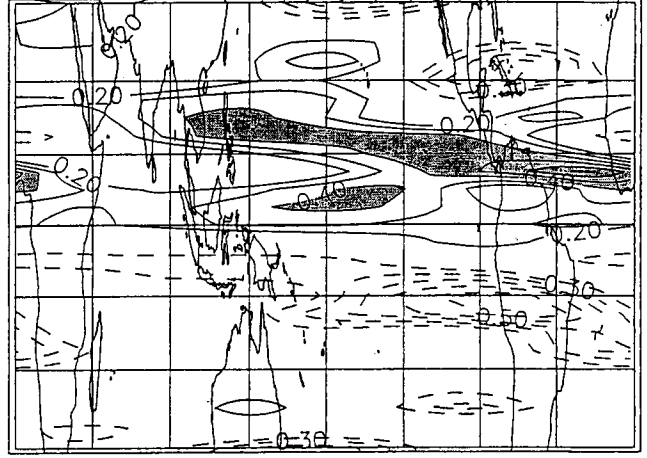
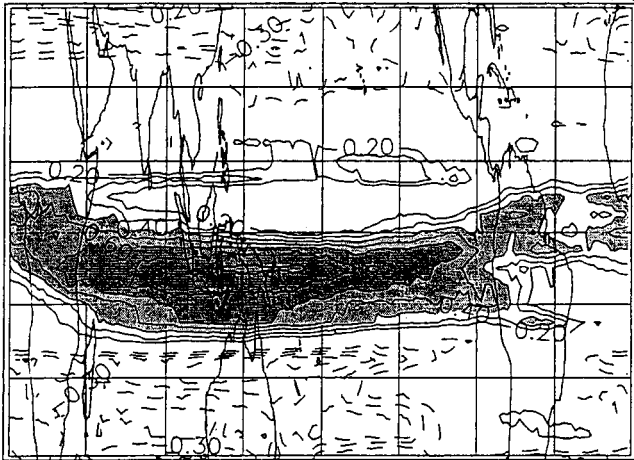
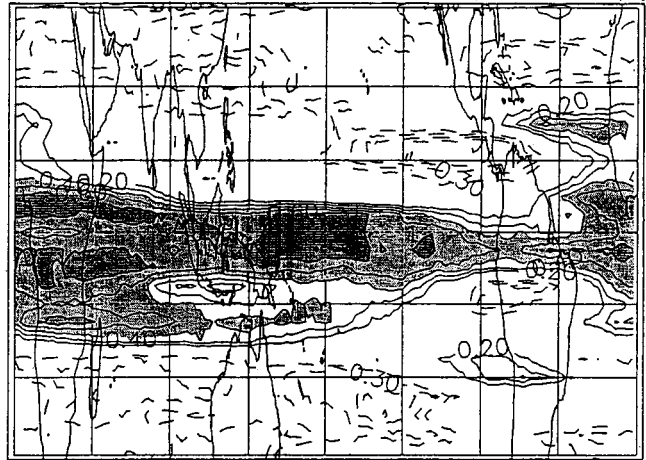


Figure 7

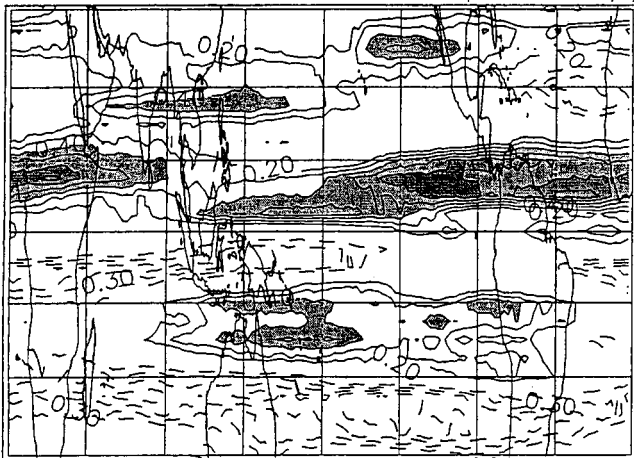
(a) inter-annual rank correlation: MJO filtered DJF OLR power and $-duv/dy$



(b) inter-annual rank correlation: MJO filtered MAM OLR power and $-duv/dy$



(c) inter-annual rank correlation: MJO filtered JJA OLR power and $-duv/dy$



(d) inter-annual rank correlation: MJO filtered SON OLR power and $-duv/dy$

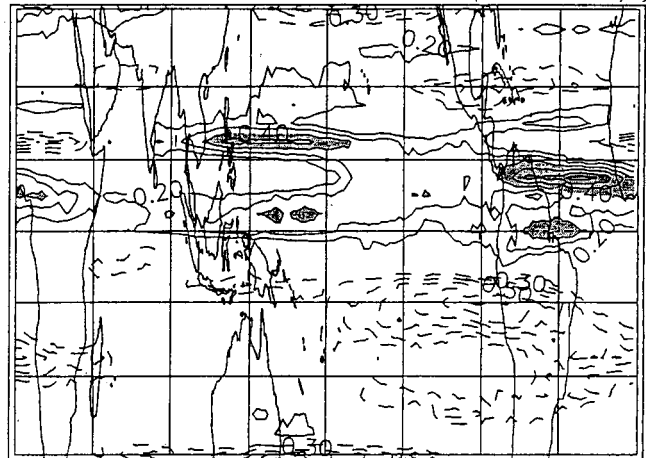


Figure 8

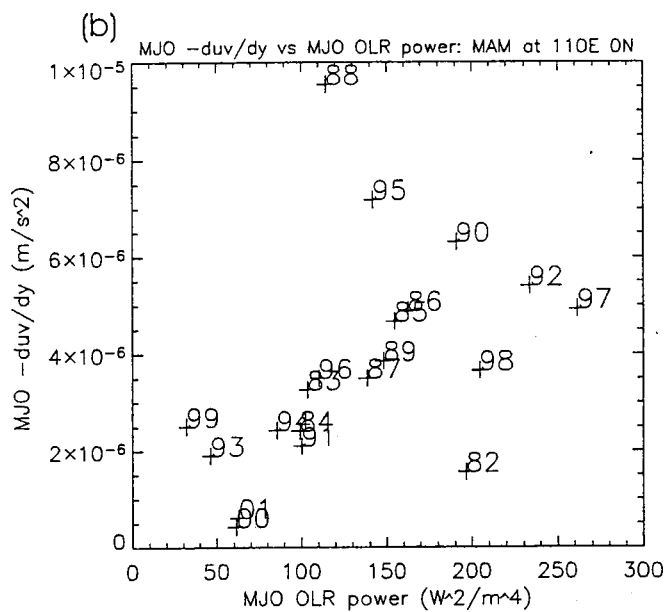
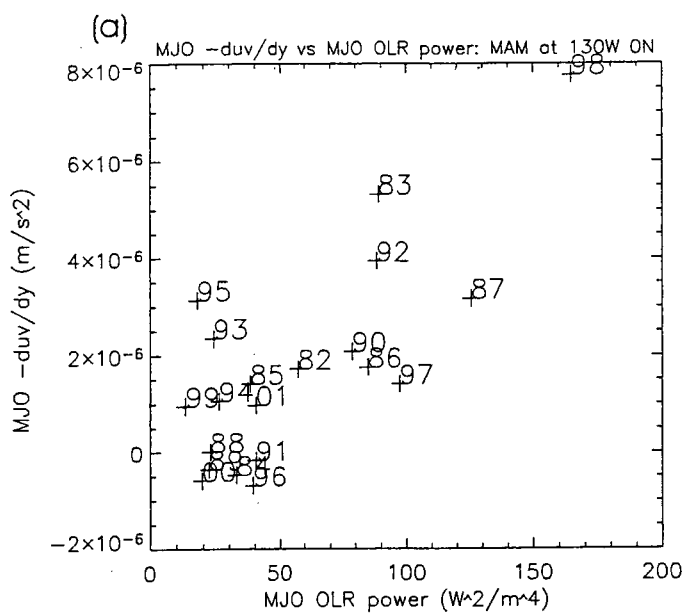


Figure 9

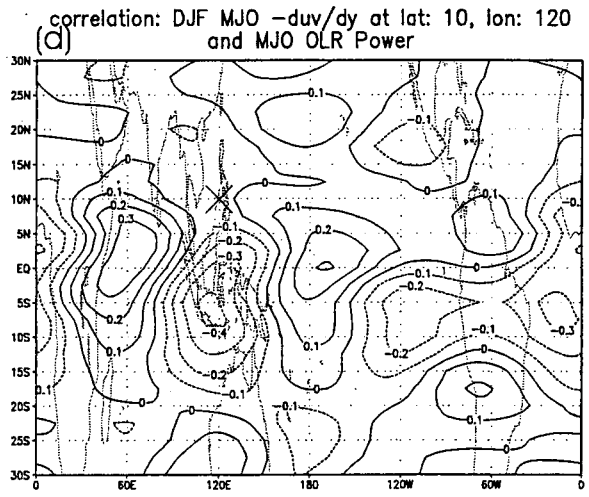
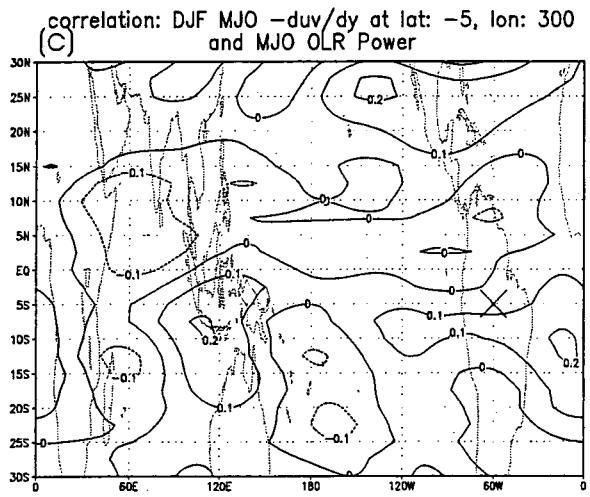
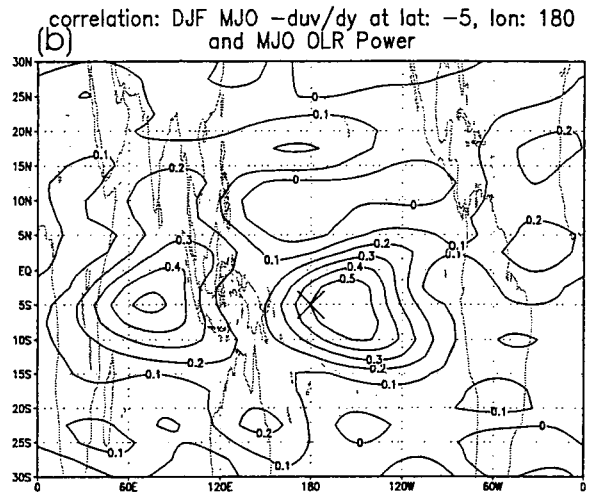
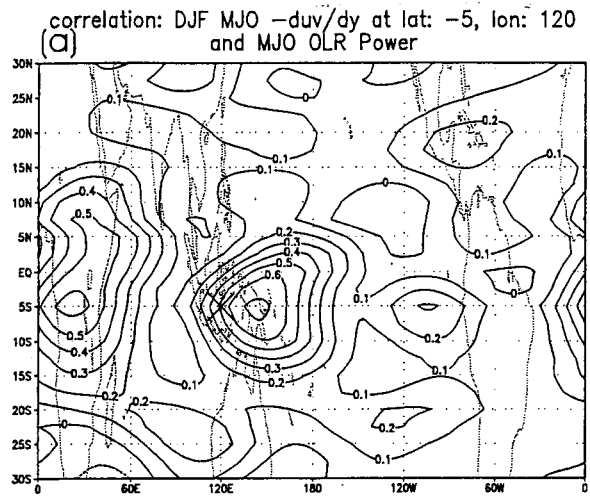


Figure 10

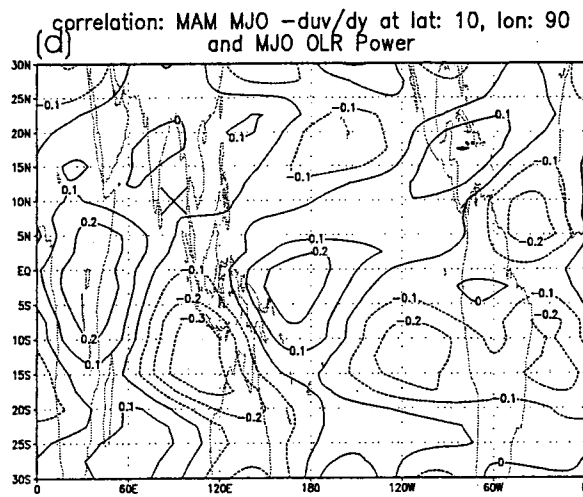
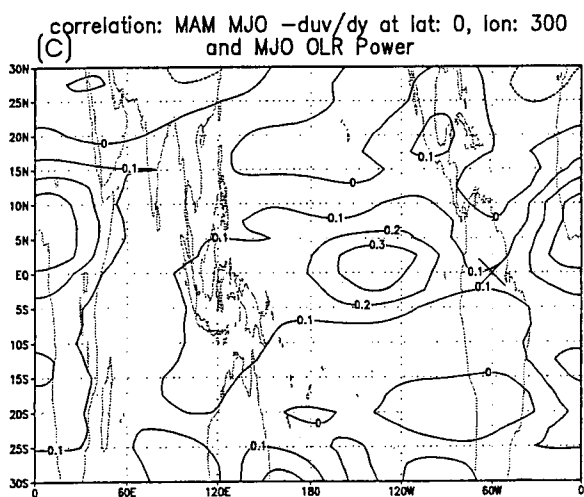
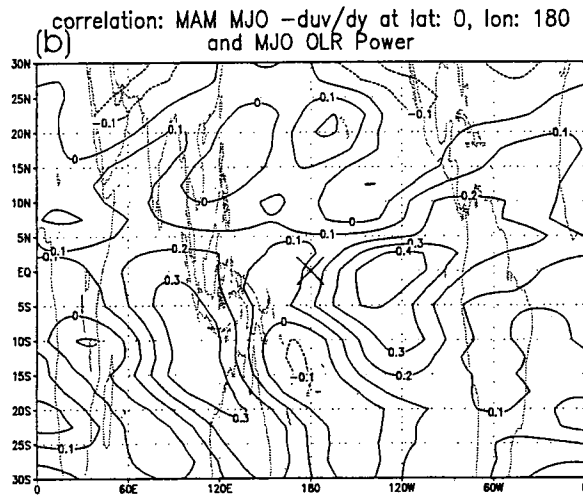
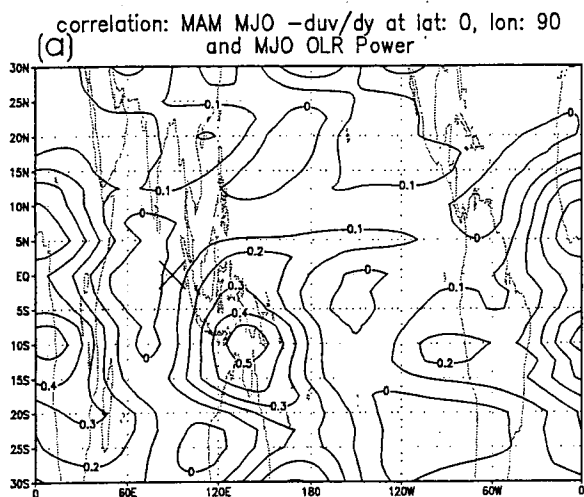


Figure 11

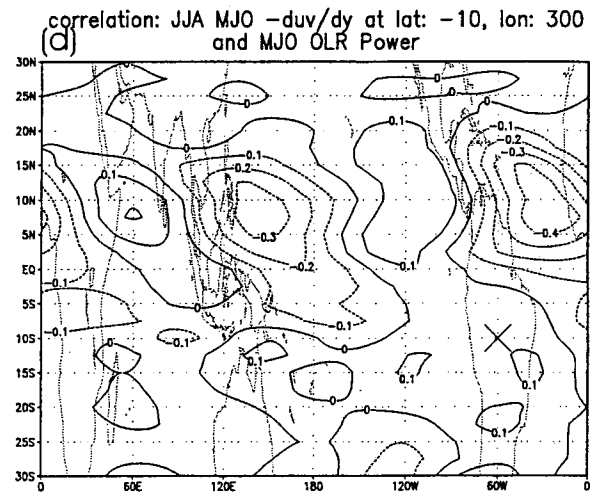
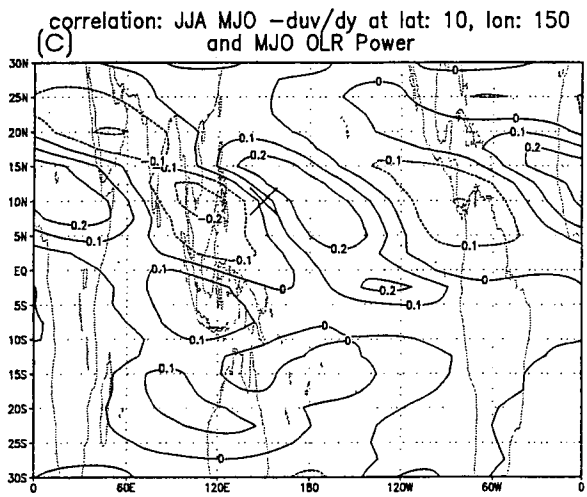
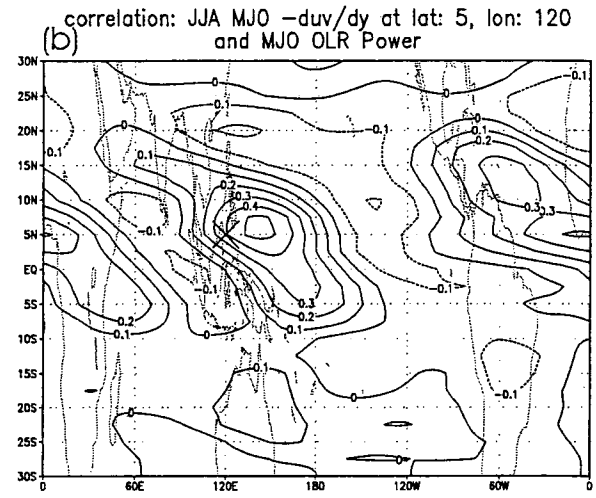
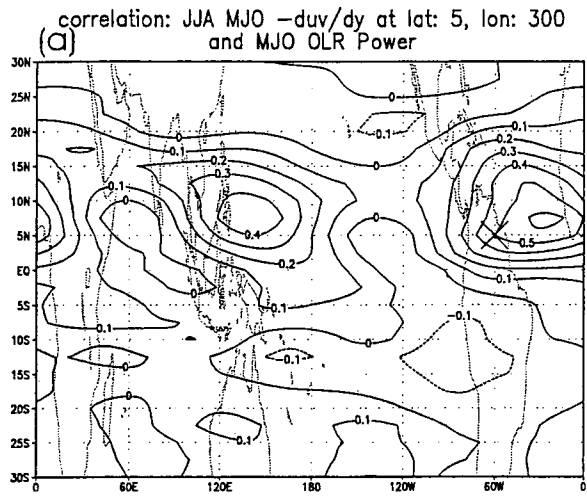


Figure 12

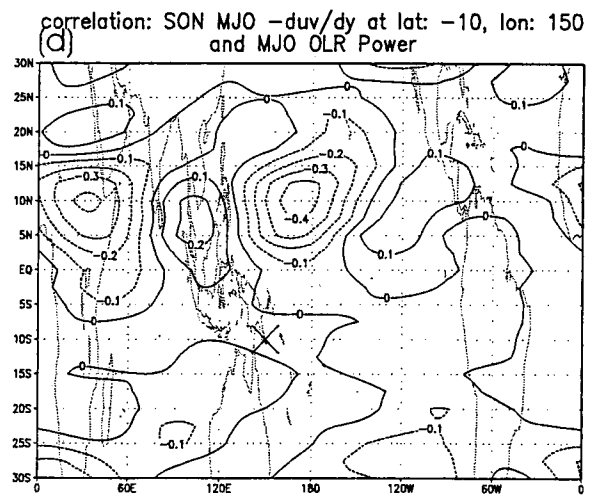
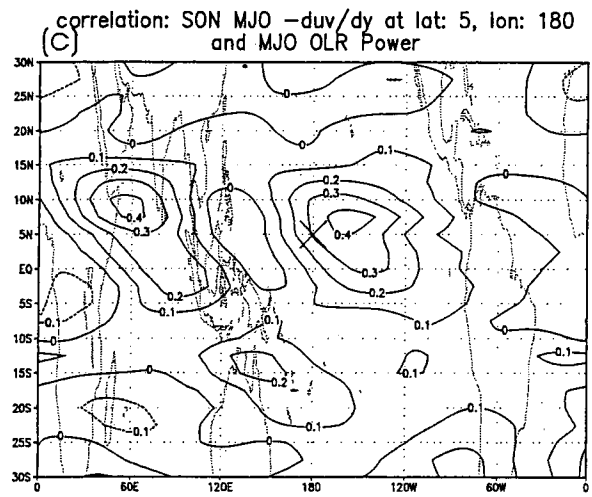
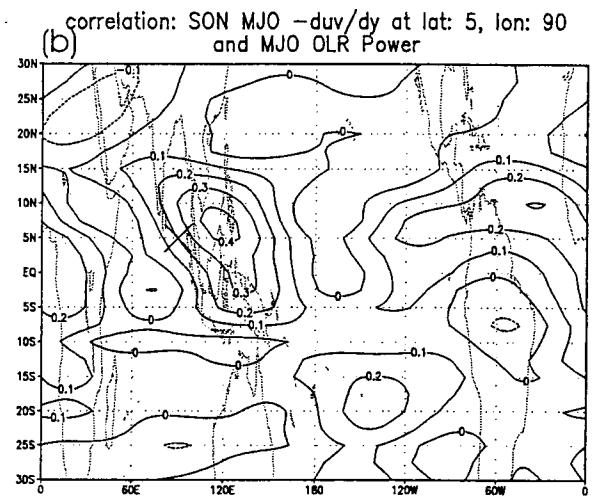
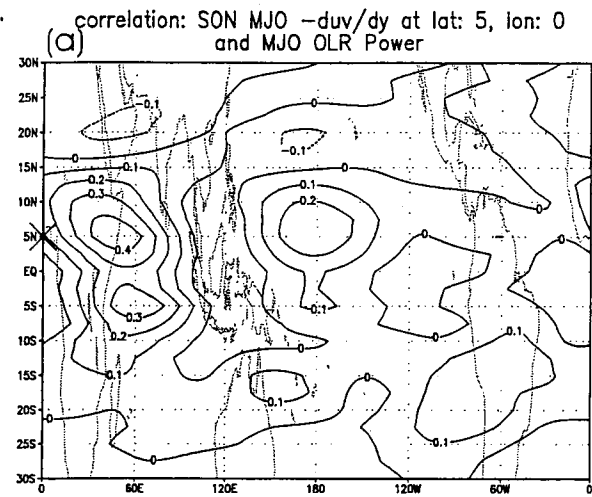


Figure 13

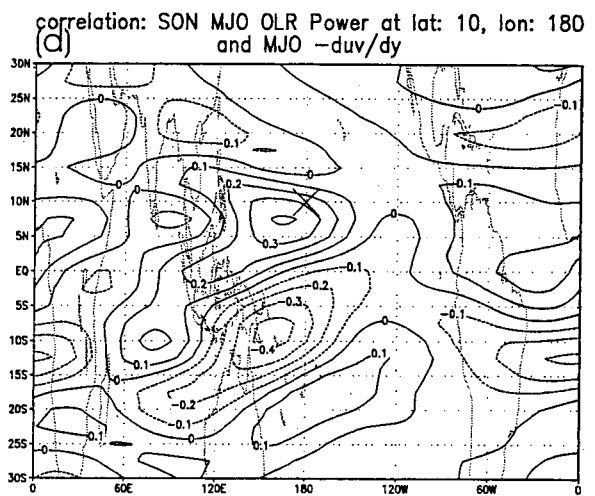
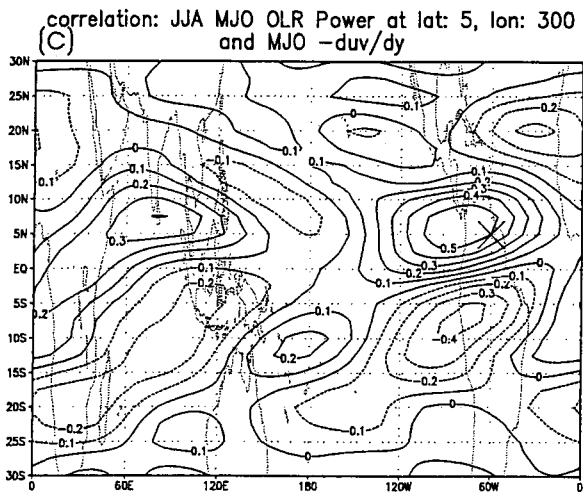
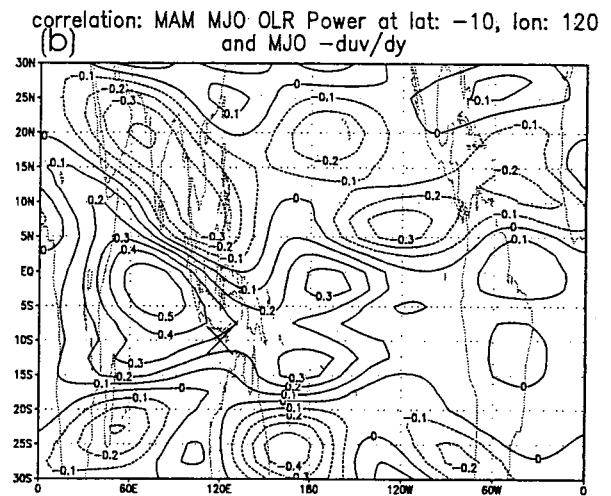
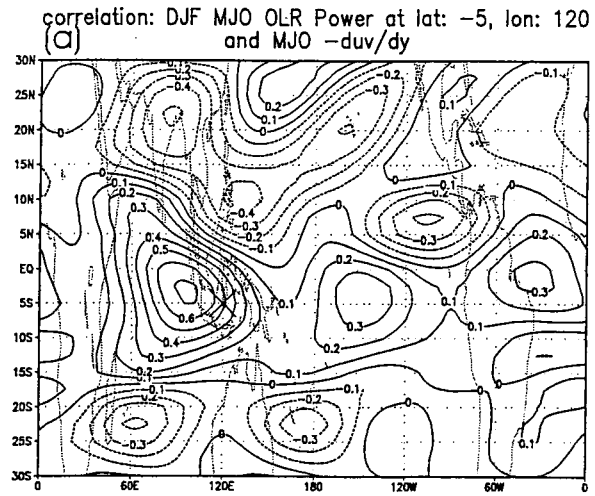


Figure 14